A multi-omic atlas of human autonomic and sensory ganglia implicates cell types in peripheral neuropathies

Lite Yang[1,2*], Adam J. Dourson[1], Ruichen Tao[1], Kevin Boyer[3], Pauline Meriau[3], John Del Rosario[1], Jiwon Yi[1], Richard A. Slivicki[1], Zachariah Bertels[1], Maria Payne[1], Juliet M. Mwirigi[1], Prashant Gupta[1], John Lemen[4], Bryan A. Copits[1], Guoyan Zhao[3], Valeria Cavalli[3], Alexandar Chamessian[1], Robert W. Gereau IV[1,3*]

1. Washington University Pain Center, Department of Anesthesiology, Washington University School of Medicine, St. Louis, MO, United States

2. Neuroscience Graduate Program, Division of Biology & Biomedical Sciences, Washington University School of Medicine, St. Louis, MO, United States

3. Department of Neuroscience, Washington University School of Medicine, St. Louis, MO, United States

4. MidAmerica Transplant, St. Louis, MO, United States

* Correspondence: lite@wustl.edu (L.Y.), gereaur@wustl.edu (R.W.G.)

ABSTRACT

The human peripheral nervous system (PNS) consists of many ganglia, including sympathetic ganglia (SG) and dorsal root ganglia (DRG), that house the cell bodies of many constituent neuron types and non-neuronal cells of the PNS. However, the molecular and cellular diversity of these human PNS cell types and their implications in human diseases remain elusive. By generating an integrated single-cell multi-omic atlas of human SG and DRG, we provide comprehensive transcriptional and epigenomic landscapes of various cell types in these peripheral ganglia. While the major cell types and their transcriptional and epigenomic features are similar between human SG and DRG, we identify key transcriptional and epigenomic differences between SG and DRG cell types, highlighting the distinct molecular mechanisms underlying their specific functions. Moreover, by mapping the expression and chromatin accessibility of disease-associated genes in human SG and DRG cell types, we identify cellular and molecular mechanisms that may underlie various peripheral neuropathies. This atlas serves as a valuable resource for understanding the intricate cell-type-specific molecules and interactions in the human PNS and their implications in human health and diseases.

INTRODUCTION

The peripheral nervous system (PNS) includes the somatic division (sensory arm, including the dorsal root ganglia [DRG] and trigeminal ganglia [TG], and motor arm) and autonomic division (sympathetic arm, including the sympathetic ganglia [SG], and parasympathetic arm). Ganglia distributed throughout the periphery house the cell bodies of many constituent neuron types and non-neuronal cells of the PNS. The SG is primarily involved in autonomic regulation, contributing to the "fight or flight" response and maintaining homeostasis, whereas the DRG plays a crucial role in sensory perception by relaying signals from the periphery to the central nervous system (CNS)[1, 2]. While SG and DRG differ in several key aspects, including innervation targets, neurotransmitter profiles, and physiological functions, they also share a common developmental origin from neural crest cells and encompass highly similar cell types[3, 4].

Sympathetic neurons, primarily noradrenergic with a smaller proportion of cholinergic neurons, innervate peripheral organs and tissues to regulate autonomic functions, such as cardiac output, blood glucose levels, body temperature, and immune responses[5]. In contrast, sensory neurons are mostly glutamatergic and transmit information about mechanosensation, temperature, pain, and proprioception from the periphery to the CNS[1, 6-8]. Morphologically, sympathetic neurons possess an axon and multiple dendrites that form synapses with the preganglionic neurons from the spinal cord, whereas sensory neurons have bifurcating pseudo-unipolar axons, projecting one branch to the target organs (skin/viscera/etc.) and the other to the CNS.

Glial cells, including satellite glial cells (SGCs) and Schwann cells, provide crucial support and regulation of the neuronal environment. Satellite glial cells contact neuronal cell bodies, whereas Schwann cells engulf the peripheral axons[9]. While Schwann cells are important for myelination, both satellite glial and Schwann cells have well-documented roles in trophic and metabolic support of neurons and regeneration[10-12]. Immune cells, such as T cells and especially macrophages (including perineural macrophages), are prevalent in the human SG and DRG[13, 14]. Various neuro-immune interactions in the DRG have been attributed to macrophages, which either promote or mitigate inflammation. DRG macrophages are thought to be a self-renewing population[15, 16], and in both ganglia, it is clear that immune cells contribute to the neuro-immune interactions that modulate neuronal functions and responses to injury[17-22]. The intricate interactions and communications between these diverse non-neuronal cell types and the neurons play essential roles in both normal physiology and disease states, underscoring the importance of the study of the cellular and molecular heterogeneity of the PNS in a high-resolution and cell-type-specific fashion.

Recent advancements in single-cell sequencing technologies have revolutionized our understanding of the diverse cell types present in the PNS primarily using model animals [4, 14, 23-29], and their unique molecular characteristics underlying health and diseased conditions [19, 20, 23, 26, 27, 30]. However, understanding the molecular and cellular diversity of human PNS is hindered by unique challenges. In this study, we present an integrated single-cell multi-omic atlas of human lumbothoracic paravertebral SG and DRG using single-nucleus multiome sequencing (snMultiome-seq, combinatorial snRNA-seq and snATAC-seq [Assay for transposase-accessible chromatin using sequencing] from the same nuclei). By analyzing SG and DRG tissues from multiple donors, we delineate the transcriptional and epigenomic landscapes of various cell types in these peripheral ganglia and their evolutionarily conserved and divergent features. We also identify key transcriptional similarities and differences in each cell type between SG and DRG, and the genomic regulatory networks that govern cell-type-specific gene expression in these peripheral ganglia. Our study offers new perspectives on the potential roles of diverse human PNS cell types in healthy biological systems and human diseased conditions broadly affecting various PNS tissues, such as hereditary sensory and autonomic neuropathies (HSAN).

RESULTS

High-quality human tissues enabled multi-omic profiling of human peripheral ganglia at single-cell resolution

Technical advancements in recent years have revolutionized our ability to understand the cellular and molecular diversity of the PNS in animal models, but multi-omic profiling of the human PNS has been hampered by unique challenges. Access to high-quality human tissues is limited, especially specimens with certain human diseases and pathologies. Some of the existing tissues may not be ideal for single-cell multi-omic profiling, as progressive post-mortem RNA degradation and chromatin integrity loss can occur within a few hours and may be exacerbated by suboptimal extraction and storage conditions during the tissue procurement process[26, 31-33]. Moreover, profiling human PNS neurons is extremely difficult as they are proportionally much sparser in human tissues compared to those in rodents and primates[14, 26]. More focused approaches and collaborative efforts are necessary for a better understanding of the neuronal heterogeneity of human PNS [25, 34-36].

To address some of these challenges, we developed a human tissue procurement pipeline at Washington University in St. Louis, where we collaborate with Mid-America Transplant to collect various PNS tissues from organ donors [37]. In most cases, donor tissues are extracted and processed within one to three hours of cross-clamp. The high viability of the tissues enables both cell culture-based experiments[37-39] and molecular assays[14]. Frozen human PNS tissues derived from our tissue procurement pipeline exhibit high integrity of their RNA contents (RNA integrity number [RIN]: 8.1 ± 0.4, n=9) and chromatin (Figure S1A, n=8), allowing single-cell multi-omic profiling of human PNS.

A transcriptional and epigenomic atlas of human SG

To study the gene expression and chromatin accessibility of individual cell types present in human SG, we performed snMultiome-seq of lumbothoracic paravertebral SG from seven individuals (five males and two females) and generated eight snMultiome-seq libraries (Figure 1A, Table 1). After quality control processes and removal of low-quality and doublet nuclei (Methods), 52,634 nuclei were retained in the final dataset with an average of 30,697 paired reads sequenced and 1,810 genes detected per nucleus for the snRNA-seq libraries (Figure S1B) and 28,208 paired reads sequenced and 7,397 high-quality transposase-sensitive fragments for the snATAC-seq libraries. The transposase-sensitive fragments detected in the snATAC-seq libraries followed the expected nucleosomal size distribution (Figure S1A) and formed 139,026 peaks when aggregated across all snATAC-seq libraries.

To identify transcriptionally defined human SG cell types, we first performed dimension reduction and clustering of the snRNA-seq data. Notably, nuclei from individual libraries were represented in each cluster, indicating minimal batch effect (Figure S1C-D). Clustering analysis revealed 11 major transcriptional cell types, including two neuronal cell types and nine non-neuronal cell types (Figure 1B,C), which are consistent with those previously described in humans and mice[4, 28, 35]. These cell types exhibit distinct transcriptional profiles and are labelled by distinct expression of 11,588 cell-type-specific marker genes (Log2FC > 1 and FDR < 0.05, Table 2). Among them, we found two neuronal cell types making up 1.4% of the total population: noradrenergic neurons (Neuronal-NA) and cholinergic neurons (Neuronal-CH). Both neuronal cell types highly express genes important for synaptic neurotransmitter release, such as *SNAP25* (Synaptosome Associated Protein 25) and *SYT1* (Synaptotagmin 1, Figure S1E), and gene ontology (GO) analysis showed that their marker genes are associated with biological processes related to key neuronal functions, such as regulation of membrane potential and synaptic transmission (Figure S1G). The noradrenergic neurons express a high level of *TH* (Tyrosine Hydroxylase) and *DBH* (Dopamine Beta-Hydroxylase), both of which are essential for norepinephrine production (Figure 1C). The cholinergic neurons express *ACHE* (Acetylcholinesterase) and *SLC18A3* (encoding the

Figure 1 - Transcriptional and epigenomic landscape of human SG

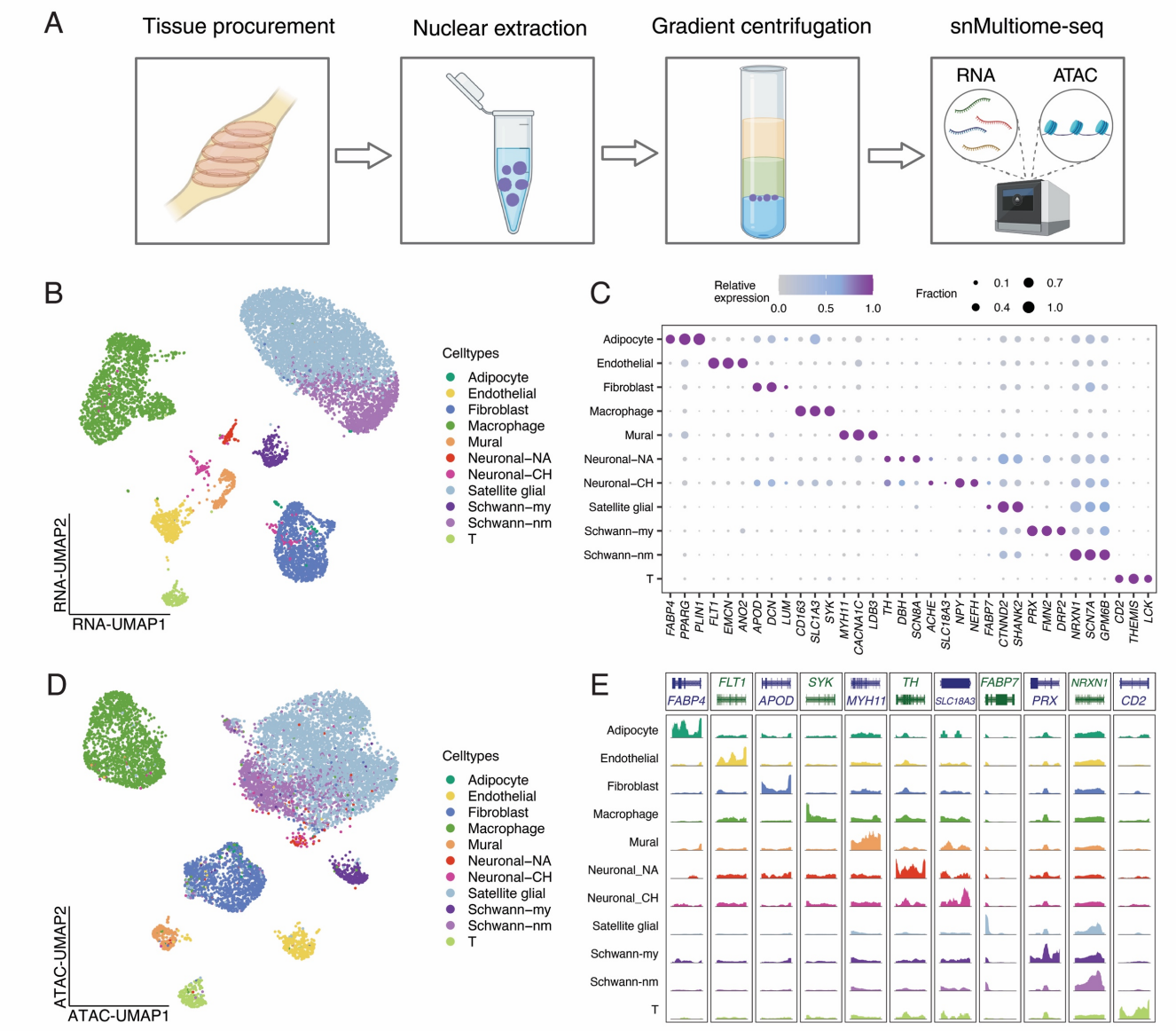

Figure 1. Transcriptional and epigenomic landscape of human SG

A. Experimental workflow of snMultiome-seq of human SG. **B**. Gene expression UMAP of human SG based on snRNA-seq data. 10,000 nuclei were randomly sampled and colored by transcriptional cell types. **C**. Dot plot displaying the expression of select marker genes in individual cell types. Dot size denotes the fraction of nuclei expressing a marker gene (>0 counts), and color denotes relative expression of a gene in each cell type (calculated as the mean expression of a gene relative to the highest mean expression of that gene across all cell types). **D**. Chromatin accessibility UMAP of human SG based on snATAC-seq data. 10,000 nuclei were randomly sampled and colored by transcriptional cell types. **E**. Coverage plot showing the accessibility around genomic loci of canonical cell-type-specific marker genes in each transcriptional cell type. The chromatin accessibility is displayed as the relative frequency of sequenced DNA fragments for each cell type, grouped by 50 bins per displayed genomic region. The frequency is normalized by the maximal frequency per genomic region.

vesicular acetylcholine transporter), genes crucial for cholinergic neurotransmission (Figure 1C). The cholinergic neurons are also noradrenergic, as 61.3% and 57.5% of *ACHE*+ nuclei in the cholinergic cluster co-express *TH* and *DBH*, respectively (Figure S1F), but the expression of *TH* and *DBH* is at a lower level in the cholinergic cluster compared to the nonandrogenic cluster. Notably, cholinergic neurons also express *NEFH*, encoding neurofilament heavy chain, suggesting their axons may be myelinated, whereas *NEFH* expression in noradrenergic neurons is much lower. Our identification of the

129 transcriptionally distinct noradrenergic and cholinergic SG neurons is largely consistent with those
130 previously reported in both humans and mice[4, 28, 35].

131 Among the nine non-neuronal human SG cell types, we found three glial cell types, including
132 satellite glial cells, myelinating (Schwann-my), and non-myelinating Schwann cells (Schwann-nm, Figure
133 1B-C). The satellite glial cells express a high level of *FABP7* (Fatty Acid Binding Protein 7), a satellite
134 glial marker gene previously reported in peripheral ganglia across species [4, 14]. Myelinating Schwann
135 cells express *PRX* (Periaxin), an essential gene for the maintenance of peripheral nerve myelin, and non-
136 myelinating Schwann cells express *NRXN1* encoding Neurexin 1, a cell adhesion molecule important for
137 the formation and function of synapses and a marker gene for non-myelinating Schwann cells. These
138 glial cell types have distinct roles in supporting, protecting, and regulating the microenvironment of PNS
139 neurons [10, 40, 41]. Consistent with this notion, we found their marker genes are associated with
140 biological processes, such as synaptic regulation, ion transmembrane transport, axon guidance and
141 myelination, as well as extracellular matrix organization and cell adhesion (Figure S1G). Moreover, we
142 also found endothelial cells expressing *FLT1*, fibroblasts expressing *APOD*, mural cells expressing
143 *MYH11*, adipocytes expressing *FABP4*, as well as immune cells, such as *SYK*-expressing macrophages
144 and *CD2*-expressing T cells (Figure 1B-C). The marker genes expressed in these cell types are also
145 associated with their unique functions in the human SG (Figure S1G). All major cell types are present in
146 each library except for adipocytes derived from a subset of donors (Figure S1D), which are likely due to
147 the inclusion of surrounding tissues in those samples during the tissue procurement and processing.

148 To study the chromatin accessibility profiles of human SG cell types, we performed dimension
149 reduction and clustering of the snATAC-seq data generated from the same nuclei in snRNA-seq, which
150 generated 26 epigenomically distinct clusters. While most cell types were nicely represented on the
151 UMAP, clustering of satellite glial cells appeared to be largely driven by donor-specific variations (Figure
152 S2A), likely reflecting differences underlying the donors' history, or the technical variation during tissue
153 procurement and sequencing process. Expectedly, when we compared the chromatin accessibility of
154 snATAC-seq peaks across donors, 46.2% of the total peaks were not shared across most donors (Figure
155 S2C). To control for the donor variability, we next corrected the chromatin accessibility analysis by
156 excluding donor-specific peaks from the analysis, resulting in an improved clustering with reduced bias
157 against libraries and donors (Figure S2B). The chromatin accessibility exhibited a high level of correlation
158 with the gene expression, as 88.4 ± 12.3% of nuclei in each snATAC-seq cluster are from the same
159 transcriptional cell types previously assigned (Figure S2D). To harmonize the cell type annotation and
160 streamline analyses, we subsequently grouped nuclei by transcriptional cell types for all downstream
161 analyses. The cell types display unique epigenomic profiles (Figure 1D) and distinct chromatin
162 accessibility around the genomic loci of canonical marker genes (Figure 1E). We identified 43,496 cell-
163 type-specific peaks (Log2FC > 1, FDR < 0.05, Table 2) in human SG cell types.

164 **Putative sex difference in SG cell types**

165 Several sex-specific differences in human autonomic functions have been previously
166 described[42-44], which prompted us to investigate whether these differences may be driven by unique
167 transcriptional and epigenomic features in the SG between males and females. In our snMultiome-seq
168 data, the overall cell type composition and cell-type-specific transcriptional and epigenomic landscapes
169 are largely similar between male and female SG (Figure S3A,B). Male and female libraries exhibit similar
170 cell type distribution (Figure S3C), and strong correlation in gene expression (Pearson's r = 0.95 ± 0.05
171 per cell type) and chromatin accessibility (r = 0.74 ± 0.18) in individual cell types.

172 Despite the similarity, differential expression analysis comparing nuclei of the same cell type
173 between the sexes revealed 82 genes significantly enriched (Log2FC > 1, FDR < 0.05) in males and 50

genes enriched in females (Figure S3D, Table 3). The most common sex differences across cell types are known sex-specific genes involved in X inactivation (such as *XIST* and *TSIX*) or are Y chromosome genes (such as *KDM5D*, *UTY*, and *DDX3Y*). Consistently, differential chromatin accessibility is also observed in genomic loci of these known sex-specific genes between nuclei from male and female donors (Figure S3E). In addition, we also identified differentially expressed genes in individual cell types between the sexes (Figure S3E, Table 3). For example, the expression of *NPY* (Neuropeptide Y), important for stress response, is trending higher in all female cell types compared to male cell types, and it is 9.5-fold significantly higher in female endothelial cells compared to male endothelial cells. Sex differences in the NPY system have been described, where it is generally higher in males than in females. However, its expression decreases as males age, whereas it shows increased expression in aged females [45]. The expression of *GRM7*, which encodes metabotropic glutamate receptor 7 (mGlu7), in cholinergic neurons is 6.7-fold higher in males than in females. *GRM7* is broadly expressed in the CNS and is important for modulating neurotransmitter release, but its sex-specific expression and potential functions in the PNS have not been reported. We also identified 278 male-specific peaks and 75 female-specific peaks (Log2FC > 1, FDR < 0.05) that may underlie sex-specific transcription regulation (Table 3). These putative transcriptional and epigenomic sex-specific features may contribute to the sex-specific SG functions. Given the small donor numbers for each sex in our snMultiome-seq data, future studies will be required to validate these putative sex-specific features.

Transcriptional conservation between human and mouse SG

Understanding the molecular and cellular convergence and divergence of SG is crucial, as the species-specific features may contribute to species-specific functions, and potentially undermine the animal models of human disease and confound the study of human biology. Despite recent advances in single-cell transcriptomics that have enabled the molecular characterization of mouse SG cell types, it remains unclear to what extent the SG cell types and their cell-type-specific molecules are evolutionarily conserved. To directly address this, we compared our human SG snRNA-seq data to that derived from mouse superior cervical SG previously reported[4]. When performing clustering without integration, the data are separated by species (Figure S4A), likely due to a combination of species-specific differences and technical variations (e.g., different sample collection procedures and sequencing techniques). To better compare the cell types present in humans and mice, we integrated the two datasets based on their shared variable features. After integration, nuclei of the same cell types from the two species were clustered together (Figure 2A) and resulted in highly similar cell type correspondence (88.6% ± 12.8% per cell type, Figure 2B). As a result, the mouse neurons are transcriptionally more similar to human noradrenergic neurons compared to cholinergic neurons (Figure S4B).

To gain insight into the evolutionary conservation of SG at the molecular level, we next compared the cell type-specific transcriptional profiles in individual SG cell types between humans and mice. The overall transcriptional profile in individual cell types is largely similar, as the expression levels of cell type-specific marker genes are highly correlated between human and mouse SG ($r = 0.79 \pm 0.08$ per cell type). In addition, 57.7 – 75.8% of the cell-type-specific marker genes in each cell type had similar expression levels between human and mouse (less than two-fold difference between the species, Figure 2C). We also observed very similar gene expression patterns for physiologically relevant genes encoding key neuropeptides and receptors, G-protein coupled receptors (GPCRs), and ion channels between human and mouse SG cell types (Figure 2E).

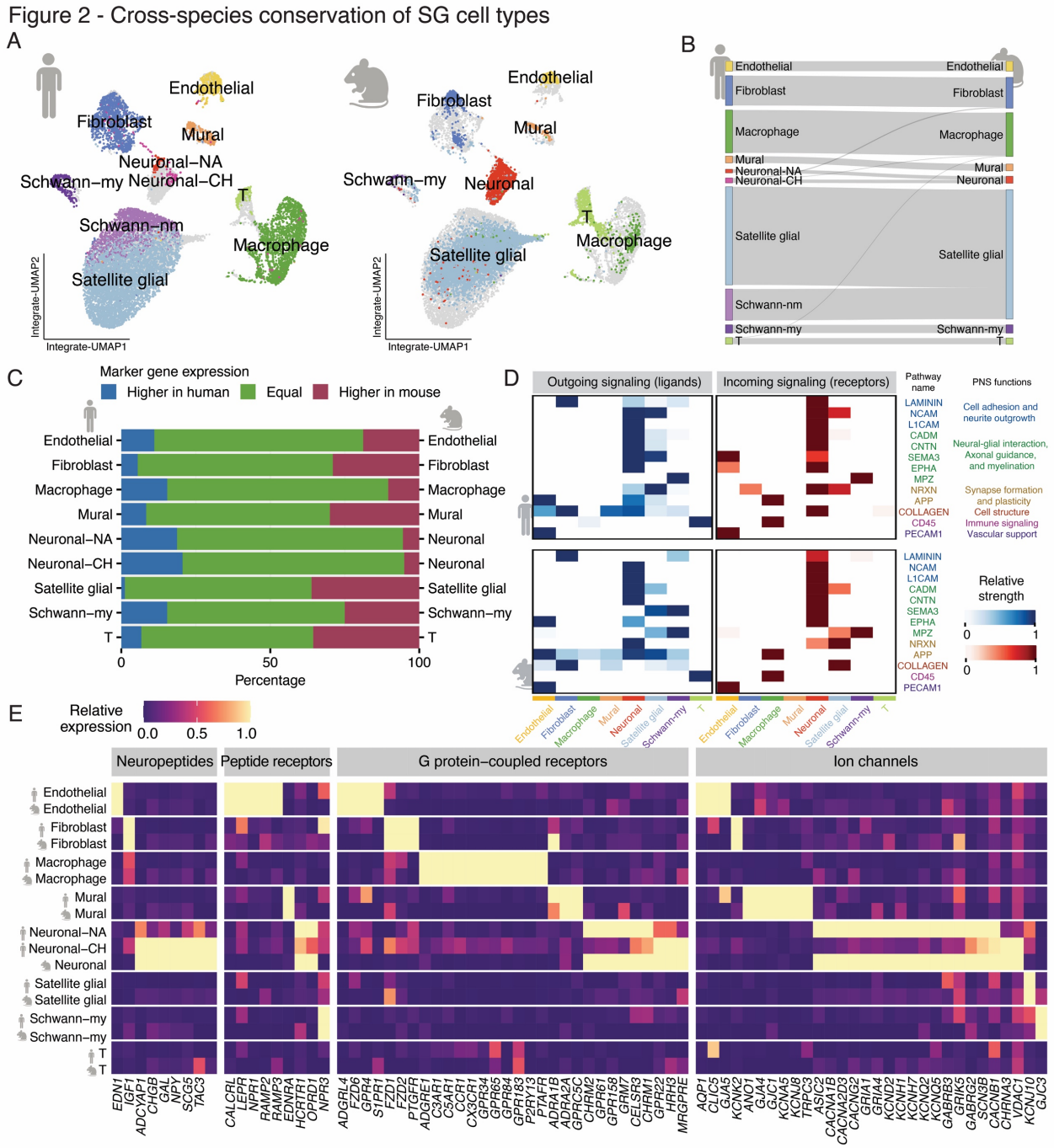

Figure 2. Cross-species conservation of SG cell types

A. Integrative gene expression UMAP of the human and mouse SG based on snRNA-seq data. 10,000 nuclei were randomly sampled per species. Left: human nuclei are colored by cell types. Right: mouse nuclei are colored by cell types previously reported. **B**. Sankey plot showing the similarities between human and mouse SG cell types. Gray lines connect the human cell types (left) to the previously reported mouse classifications (right) they are most closely related, quantified as the human nuclei in each cell type co-clustered to the respective mouse cell types when the two datasets were integrated. **C**. Bar plot showing the percentage of cell-type-specific marker genes for each cell type grouped by their expression level in human and mouse. Pair-wise differential expression analysis was done comparing nuclei of the same cell type between human and mouse, genes with Log2FC >1 and FDR < 0.05 are higher in human, genes with Log2FC < (-1) and FDR < 0.05 are higher in mouse, and all other genes are equally expressed in two species **D**. Heatmap showing the relative strength of conserved signaling pathways across individual human (top panels) and mouse (bottom panels) cell types. **E**. Heatmap displaying the expression of select cell-type-specific physiologically revelent genes in individual human and mouse SG cell types. Color denotes relative expression of a gene in each cell type of each species (calculated as the mean expression of a gene relative to the highest mean expression of that gene across all cell types of a given species).

Moreover, to compare the cell-cell communications in human and mouse SG, we performed ligand-receptor analysis on each dataset separately. To control the effect of technical variation, such as sample size and sequencing depth, we downsampled the cell number and UMI counts in each human SG cell type to match their mouse counterparts (Methods). In total, we identified 28 and 26 significantly enriched signaling pathways in human and mouse SG, respectively (Methods). Among them, 13 signaling pathways are shared between species (Figure 2D). These evolutionarily conserved pathways are associated with important SG cell functions such as neurite outgrowth, myelination, and synaptic functions, and several genes have been implicated in various human diseases. For example, APP (amyloid precursor protein) and NCAM (Neural cell adhesion molecule) signaling pathways are crucial for neuronal development and synapse formation in the nervous system[46-48]. In both human and mouse SG, *APP* is expressed in both neurons and non-neuronal cell types, such as satellite glial cells and fibroblasts (Figure 2D, S5A,E,F). NCAM ligands *NCAM1*, *NCAM2*, and the receptor *L1CAM* are expressed in SG neurons in both species, whereas *NCAM1* and *NCAM2* are also expressed in satellite glial cells and Schwann cells in humans but not in mice (Figure 2D, S5B,E,F). CNTN (Contactin) and LAMININ play physiological roles in axonal and cellular structural support, and *CNTN1* and *LAMA2* are expressed in various SG cell types in humans and mice (Figure 2D, S5C-F). Abnormality of APP and NCAM in the SG has been reported in animal models of neurodegenerative disorders, such as dementia [49], and *CNTN1* and *LAMA2* are the underlying genetic causes of specific types of congenital muscular dystrophies[50, 51]. However, little is known about the links between the molecular dysfunctions in the SG to the autonomic dysfunctions commonly observed in these neurodegenerative disorders. This analysis explores the potential molecular and cellular basis of SG that may be affected and conversely contribute to the autonomic dysregulations reported in human diseases[52, 53], and sheds light on the evolutionary conservation that would aid the future investigation of human diseases using animal models.

Transcriptional divergence of human and mouse SG

Despite the overall conservation of the cell types and their cell-type-specific molecular features between human and mouse SG, we also observed some differences between the two datasets that may underlie some species-specific SG functions. First, the abundance of neuronal populations in mice is 14.2 times higher than that in humans (Figure S4C). The lower relative abundance of neurons vs. non-neuronal cells in human SG is consistent with previous studies of peripheral ganglia[14, 26]. We also observed proportionally more abundant macrophages in humans than in mice (Figure S4D), which is consistent with previous cross-species comparison of peripheral ganglia and may contribute to species-specific neuro-immune interactions[25, 26]. Interestingly, the mouse data of superior cervical SG lack transcriptional clusters representing non-myelinating Schwann cells and cholinergic neurons, which may be due to species-specific differences or ganglion level-specific differences. In addition, we found 1,010 genes differentially expressed between human and mouse SG cell types, including 18 physiologically relevant genes more highly expressed in human cell types, and 30 physiologically relevant genes more highly expressed in mouse cell types (Figure S6A). Moreover, we identified 15 signaling pathways that are only significant in the human dataset and 13 signaling pathways that are only significant in the mouse dataset (Figure S6B,C). Among the species-specific signaling pathways, glutamate signaling is only enriched in humans (Figure S6D). *SLC1A3* (encoding the Excitatory Amino Acid Transporter 1) is distinctly expressed in human macrophages. *GRIK2* and *GRIK3*, which encode the Glutamate Ionotropic Receptor Subunits 2 and 3, respectively, are expressed in human SG neurons and non-neuronal cells, such as endothelial cells, fibroblasts, satellite glial cells, and Schwann cells. However, *Slc1a3*, *Grik2*, and *Grik3* are not significantly expressed (< 5% nuclei per cell type) in any mouse cell types. Serotonin/dopamine signaling is only enriched in mice (Figure S5E). *Ddc* (Dopa Decarboxylase) and *Htr3a* (encoding 5-Hydroxytryptamine [serotonin] Receptor 3A) are highly expressed in mouse SG neurons, while not significantly expressed in any human SG cell types. It's promising that some of the

differences we identified between the human and mouse SG data may be important for species-specific SG signaling. However, future studies are required to validate the species-specific differences reported in this study.

Transcriptional comparison between human SG and DRG

The sensory system in the DRG relays ascending signals from the environmental stimuli and internal organs to the CNS, while the sympathetic system relays descending signals from the CNS to the peripheral tissues for mediating the ‘‘fight or flight’’ response and maintaining body homeostasis. While both developmentally originated from neural crest cells, DRG and SG exhibit distinct innervation patterns and carry out unique physiological roles and functions. Previous studies reported that SG and DRG share similar cell types in rodents[4], but the extent of transcriptional and epigenomic similarities and differences in the human SG and DRG cell types has not been reported.

To address these questions, we integrated our snMultiome-seq data from human SG with the snMultiome-seq data from human DRG reported in a companion study [companion study]. As the tissues used in both studies were derived from the same procurement pipeline and processed using the same nuclear extraction and sequencing protocols, this allowed us to rigorously control for technical variations. Indeed, we identified overlapping cell types from the two datasets with similar cell type distribution (Figure S7A). Human SG and DRG cell types exhibit high levels of transcriptional similarity, as nuclei of the same cell types from SG and DRG co-clustered nicely on the UMAP, even before integration (Figure 3A, S7B,C), and 74.7 – 99.7% of nuclei from each SG cell type are anchored to the same DRG cell type in the integration analysis (Figure 3B). When we examined the cell type-specific transcriptional profiles, 82.8 – 98% of the cell type-specific marker genes in each cell type are expressed at a similar level (less than two-fold difference) between the two ganglia (Figure 3C). Interestingly, the human SG and DRG neuronal subtypes exhibited a high level of transcriptional correspondence. 80.1% of noradrenergic SG neurons are mapped to C-fiber DRG neurons (Figure 3B), and these two neuronal subtypes are transcriptionally more similar to each other than to other SG and DRG neuronal subtypes (Figure S7D). Out of 6,661 marker genes that are expressed in either noradrenergic SG neurons or C-fiber DRG neurons, 85.3% are expressed at similar levels between the two neuronal cell types. Noradrenergic SG neurons and C-fiber DRG neurons express ion channels and GPCRs, such as *SCN9A*, *OPRD1*, and *OPRM1* (Figure S7E). Similarly, 99.7% of cholinergic SG neurons are mapped to A-fiber DRG neurons, and they are transcriptionally more similar to each other than to other SG and DRG neuronal subtypes. 87.5% of the 3,314 marker genes that are expressed in either neuronal type are expressed at similar levels between the two types. Cholinergic SG neurons and A-fiber DRG neurons both express genes associated with myelinated axons, such as *NEFL*, *NEFH*, and *NEFM*.

Despite the overall transcriptional similarity, SG and DRG cell types also exhibit some key differences that may underlie their distinct neurobiological functions. In total, we identified 348 genes more highly expressed in SG cell types and 769 genes more highly expressed in DRG cell types (Table 4). SG-enriched genes are important for autonomic regulatory function, such as regulation of vasculature, muscle contraction, and blood circulation, and the neurotransmitter release (Figure 3D). SG and DRG neurons differ in many key aspects, such as morphology, neurotransmitter release, physiology, and function, which appeared to be reflected in their gene expression patterns. Compared to DRG, SG neurons highly express genes important for norepinephrine production and signaling (e.g., *SLC18A1*, *SLC18A2*, *TH*, *DBH*, *SLC6A2, and DDC*), and cholinergic signaling (e.g., *CHRNA3* and *CHRNA8* encoding subunits of the nicotinic acetylcholine receptor genes,

Figure 3 - Comparison between human SG and DRG

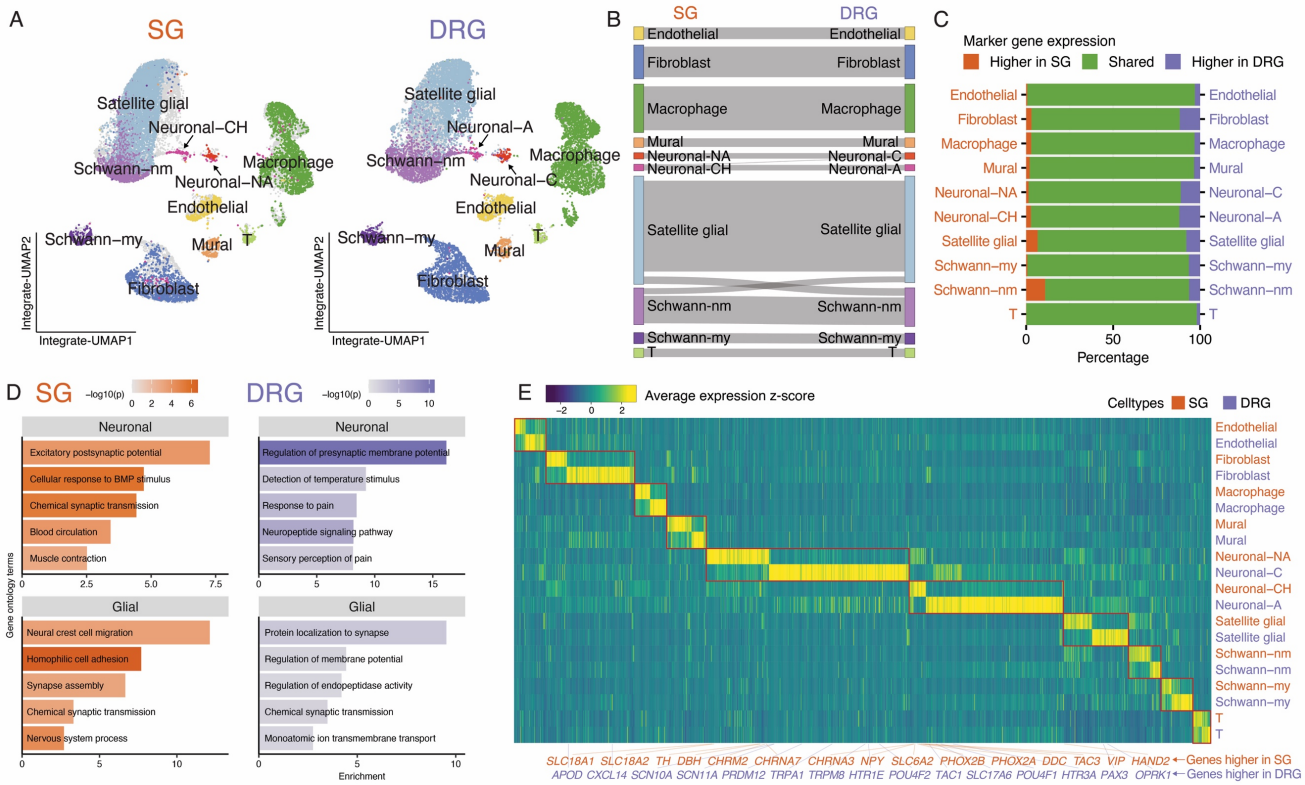

Figure 3. Comparison between human SG and DRG

A. Integrative gene expression UMAP of the human SG and DRG based on snRNA-seq data. Left: SG nuclei are colored by cell types, and DRG nuclei are displayed in the background as grey dots. Right: DRG nuclei are colored by cell types previously reported, and SG nuclei are displayed in the background as grey dots. B. Sankey plot showing the similarities between human SG and DRG cell types. Gray lines connect the SG cell types (left) to the previously reported DRG cell type classifications (right) they are most closely related, quantified as the SG nuclei in each cell type co-clustered to the respective DRG cell types when the two datasets were integrated. C. Bar plot showing the percentage of cell-type-specific marker genes for each cell type grouped by their expression level in SG and DRG. Pair-wise differential expression analysis was done comparing nuclei of the same cell type between SG and DRG, genes with Log2FC >1 and FDR < 0.05 are higher in SG, genes with Log2FC < (-1) and FDR < 0.05 are higher in DRG, and all other genes are equally expressed in two species D. Plot showing the top five biological processed enriched in the GO analysis of SG and DRG. E. Heatmap displaying the expression of cell-type-specific genes that are differentially expressed between SG and DRG (See Table 4 for the original data).

and *CHRM2* encoding a subunit of the muscarinic acetylcholine receptors, Figure 3E). SG neurons also uniquely express neuropeptide genes, including *NPY* (Neuropeptide Y), *VIP* (Vasoactive intestinal peptide), and *TAC3* (encoding Neurokinin B). Genes encoding transcription factors crucial for the sympathetic cell type development and specificity, such as *PHOX2A*, *PHOX2B*, and *HAND2*, are also more highly expressed in cell types in the SG than DRG. On the other hand, DRG-enriched genes are important for the detection of environmental stimuli and sensory perceptions, including pain (Figure 3D). Compared to SG, DRG neurons highly express genes encoding ion channels for nociceptive signal transmission (e.g., *SCN10A* and *SCN11A*), temperature sensing (*TRPA1* and *TRPM8*, Figure 3E). DRG neurons also highly express *SLC17A6*, encoding a vesicular transporter of glutamate, the primary neurotransmitter released by the DRG neurons, and *TAC1*, encoding substance P, a key modulator for pain sensation[54, 55]. Neuropeptide receptor genes, such as serotonin receptors (*HTR1E* and *HTR3A*) and opioid receptor *OPRK1,* are more highly expressed cell types in DRG than SG. Sensory neuron-

specific transcription factor genes, such as *PRDM12*, PAX3, *POU4F1*, and *POU4F2,* are also more highly expressed in DRG than SG.

Glial cells exhibit distinct anatomical distribution in human peripheral ganglia

Satellite glial cells and Schwann cells are the two main types of glial cells in the PNS. Satellite glial cells encase the cell bodies of neurons, whereas Schwann cells ensheathe the axons of neurons[10, 11, 56]. A previous comparative study has shown that, in mice, the myelinating Schwann cells are sparser in the superior cervical SG compared to the lumbar DRG, whereas the satellite glial cells are similarly abundant between the ganglia[4]. However, both myelinating Schwann cells and satellite glial cells are similarly abundant in our human SG and DRG atlases, suggesting a potential cross-species difference. To validate our findings, we investigated the distribution of glial cell types in human lumbothoracic paravertebral SG and DRG using RNA fluorescent in-situ hybridization (RNA-FISH, Figure 3). We labeled myelinating Schwann cells with *PRX*, which is specifically expressed in myelinating Schwann cells according to our snMultiome-seq data (Figure 4G). In addition, we probed for *NRXN1* to label satellite glial cells and non-myelinating Schwann cells. While *NRXN1* is broadly expressed in all cell types (Figure S8A), its expression level is 5.7-fold higher in non-myelinating Schwann cells and 1.4-fold higher in satellite glial cells than in other cell types in our snMultiome-seq data. Therefore, we reasoned that *NRXN1* can preferentially label non-myelinating Schwann cells and satellite glial cells based on different expression levels (Figure 4G). Finally, we used *SNAP25*, a pan-neuronal marker, to label the neuronal population.

We performed RNA-FISH on two human SG and two human DRG samples (Table 1, Figure 4A,B), imaging and analyzing 20 neuron-enriched regions of interest (ROIs) and 20 axon-enriched ROIs (Figure 4C-F). We then segmented the cells using cellpose and quantified the expression and called positive cells using SCAMPR (Figure S8B-D)[57, 58]. In total, we identified 38,034 SG cells and 50,426 DRG cells. *PRX* labeled 13,132 (14.8%) cells and *NRXN1* labeled 14,901 (16.8%) cells. *PRX* and *NRXN1* labeled distinct populations that showed little expression of *SNAP25* (Figure 4H). When we compared their distribution across different ROIs, we found that the abundance of both *PRX*+ cells and *NRXN1*+ cells is similar between human SG and DRG (Figure 1I,J). However, *PRX*+ cells are more enriched around axon-enriched regions compared to around the neuron-enriched regions in both SG and DRG, suggesting that myelinating Schwann cells are preferentially localized around axonal bundles. While *NRXN1*+ cells are relatively equally distributed across different regions in SG and DRG, *NRXN1* expression is higher in the axon-enriched regions than neuron-enriched regions (Figure 6K). These results suggest that *NRXN1* higher-expressing non-myelinating Schwann cells may be more enriched around axons, and *NRXN1* lower-expressing satellite glial cells may be more enriched around neuronal somas. Our snMultiome-seq and RNA-FISH results collectively showed that individual glial cell types are similarly abundant between human SG and DRG, while each glial cell type may exhibit distinct anatomical distribution in relation to the neuronal soma and axons.

Genomic regulatory networks of human peripheral ganglia

While the gene expression programs in the diverse PNS cell types have been largely elucidated in animals and in some human tissues, the genomic regulatory networks (GRNs) that govern the distinct gene expression patterns in individual cell types have not yet been explored in humans. The intricate interactions between the trans-acting genomic regulatory elements (GRE, e.g., transcription factors [TF]) and cis-acting GREs (e.g., promoters, enhancers, and silencers) fine-tune the gene expression in a cell-type-specific manner. Our multi-omic atlas of the human peripheral ganglia offers a valuable resource to characterize these putative GREs that control the cell-type-specific gene expression and study the GRNs underlying the distinct identities and functions of individual human PNS cell types. Our study might also

Figure 4 - hDRG and hSG glial cells

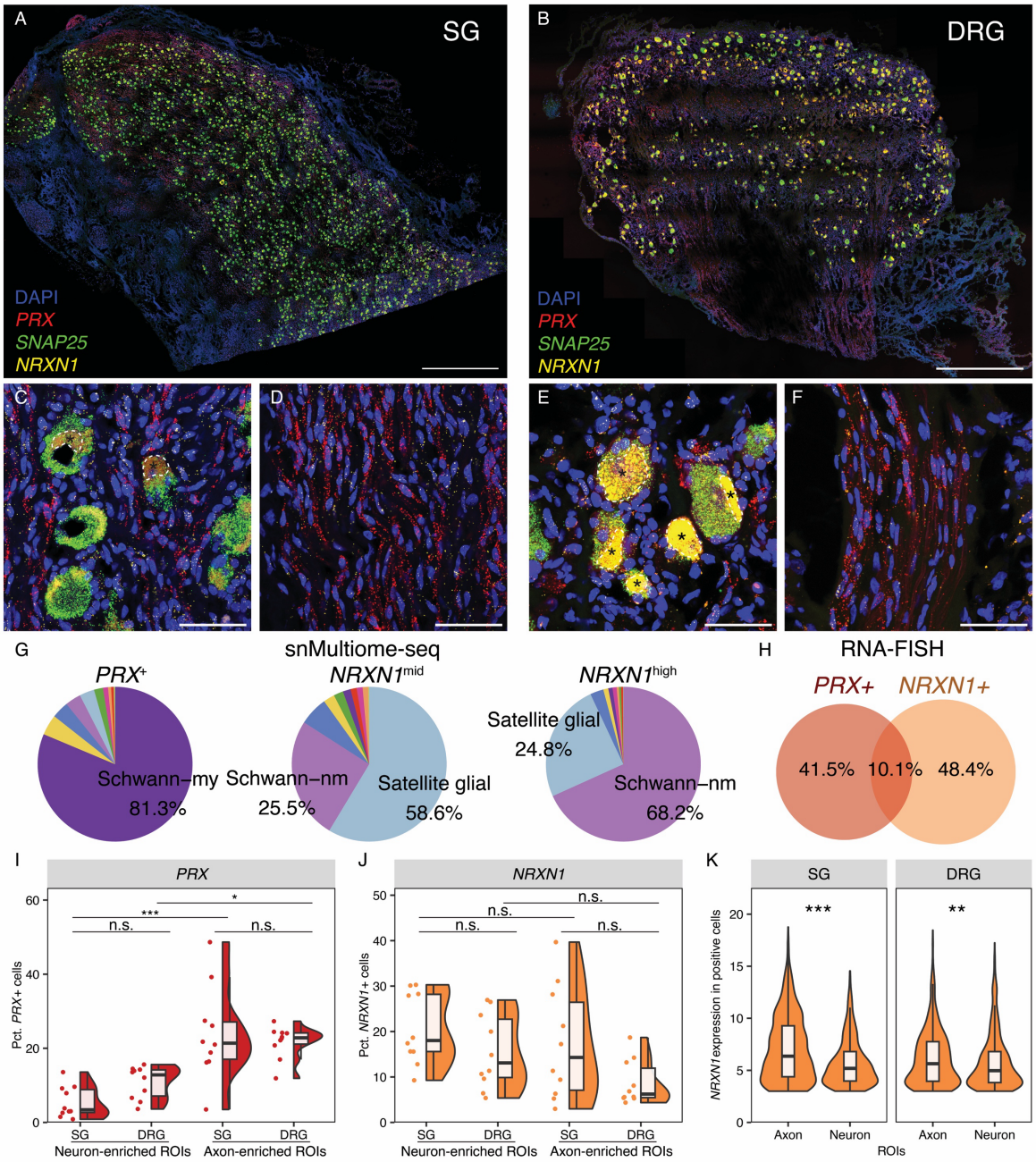

Figure 4. Glial cell distribution between human SG and DRG

A. A representative FISH image from human SG. Scale bar = 1mm. B. A representative FISH image from human DRG. Scale bar = 1mm. C and E. Representative zoomed-in images of neuron-enriched regions in human SG (C) and DRG (E). Scale bar = 50 µm. Autofluorescence from lipofuscin is circled with white dotted lines and labeled with asterisks. D and F. Representative zoomed-in images of axon-enriched regions in human SG (D) and DRG (F). Scale bar = 50 µm. G. Cell type distribution of PRX+ (> the median value among all positive nuclei) nuclei and NRXN1 mid- (> the median value and no more than 75-percentile among all positive nuclei) and high-expressing (> 75-percentile among all positive nuclei) nuclei in snMultiome-seq data of human SG and DRG. H. The overlap between PRX+ cells and NRXN1+ cells in RNA-FISH analysis. I. Quantification of PRX+ cell distribution across different ROIs. Two-way ANOVA: F (3,36) = 14.32, p = 2.6E-6 [***]. Tukey HSD tests: p = 0.38 (neuron DRG-neuron SG), p = 1.3E-5 [***] (axon SG-neuron SG), p = 0.57(axon DRG-axon SG), p = 0.014 [*] (axon DRG-neuron DRG). J. Quantification of NRXN1+ cell distribution across different ROIs. Two-way ANOVA: F (3,36) = 3.26, *p* = 0.03 [*]. Tukey HSD tests: *p* = 0.38 (neuron DRG-neuron SG), *p* = 0.83 (axon SG-neuron SG), *p* = 0.15(axon DRG-axon SG), *p* = 0.32 (axon DRG-neuron DRG). K. The distribution of *NRXN1* expression from different ROIs in human SG and DRG. One-way t-test testing if expression is higher in axon-enriched ROIs than neuron-enriched ROIs: *p* = 2.1E-28 [***] for SG, and p = 0.0015 [**] for DRG. [**p* = 0.05, ***p* = 0.001].

366 provide new opportunities for understanding the function of disease-associated genetic variations and
367 designing cell-type-specific genetic tools (e.g., transgenic mice or gene therapy vectors).

368 To study the cell-type-specific GRNs, we performed Functional Inference of Gene Regulation
369 (FigR) analysis on the snMultiome-seq data of human SG and DRG[59]. By correlating the accessibility
370 of snATAC-seq peaks with the expression of cell-type-specific genes in snRNA-seq, we were able to
371 connect the distal GREs to target genes and infer the activity of TFs that may mediate these regulatory
372 events. In total, we identified 39 TFs enriched in either human SG or DRG cell types (Figure 5A), and 25
373 are shared between the two ganglia, including 15 transcription activators, whose motif enrichment is
374 positively correlated with the expression of regulated genes, and 10 transcription repressors, whose motif
375 enrichment is negatively correlated with the gene expression (Figure 5B). For example, SOX10 (SRY-
376 Box Transcription Factor 10) is a key regulator of neural crest cell development and critical for the
377 development of satellite glial cells and Schwann cells across different PNS tissues[60-62]. Indeed, we
378 found that the SOX10 gene is highly expressed in the satellite glial cells, myelinating and non-myelinating
379 Schwann cells in both human SG and DRG, and the SOX10 binding motif is also highly enriched in the
380 same cell types (Figure 5C). We identified 354 genes putatively regulated by SOX10 (Figure 5D), and
381 they significantly overlap with cell-type-specific marker genes for satellite glial cells, myelinating and non-
382 myelinating Schwann cells (Figure S9A, Table 5). These results suggest that SOX10 may act as a fate-
383 determining TF for PNS glial cell types by activating and maintaining the expression of marker genes for
384 different glial cell types. Similarly, SPI1 (Spi-1 Proto-Oncogene, also known as PU.1) is well known for its
385 role in the development and differentiation of immune cells[63-65]. SPI1 is likely a transcription activator
386 for the SG and DRG macrophages due to its high gene expression and high motif enrichment (Figure
387 5E). The majority of the SPI1-regulated genes is uniquely expressed in macrophages (Figure 5F), and
388 SPI1 may be a key regulator for macrophage functions as its top regulated genes are associated with
389 immune processes such as inflammatory response (*SYK*, *ALOX5*, *C5AR1*, *CD14*, *TAB2*), immune
390 signaling (*THEMIS2*, *MS4A7*, *FPR3*), and pathogen recognition and processing (*NCF2*, *CTSB,* Figure
391 5G, Table 5). Besides the shared TFs between the two peripheral ganglia, we also identified eight SG-
392 specific TFs and six DRG-specific TFs (Figure S9B,D), including HAND2 (Heart And Neural Crest
393 Derivatives Expressed 2, Figure S9C), which is important for the development of autonomic nervous
394 system including the noradrenergic neurons[66, 67], and PAX3 (Figure S9E), which is pivotal for the
395 differentiation of neural crest precursor cells into sensory neurons[68, 69]. These ganglion-specific TFs
396 may be important for the development and differentiation of the human SG and DRG and may underscore
397 their unique properties and functions.

398 Interactions between neurons and the immune system are important for regulating neuronal
399 functions and have been implicated in numerous pathophysiological conditions, such as obesity and
400 chronic pain [20, 70-72]. Macrophages in the DRG are a cell type of interest since they have roles in
401 regulating neuropathic pain and the ganglia microenvironment in animal studies[22, 73], and there is a
402 population of macrophage/macrophage-like cells that is in close proximity to neurons after injury in both
403 animal models and in humans[13, 15, 16]. In our analysis, we identified six TFs that exhibited the highest
404 expression in macrophages, including those that are shared between SG and DRG (SPI1, ETV5, ETV6,
405 RUNX1, and RBPJ), and ZNF331, which exhibits much higher activity in DRG than SG. To further
406 investigate the functions of these macrophage-specific TFs, we performed subclustering of the SG and
407 DRG macrophages and identified three clusters (Figure 5H). These clusters likely represent different
408 macrophage states based on their marker genes: Mac_1 expresses anti-inflammatory markers, such as
409 *CD163* and *MRC1*, whereas Mac_2 expresses pro-inflammatory markers, such as *OLR1* and *CD83*
410 (Figure S10A). Mac_3 expresses markers of proliferation, including *TOP2A, MKI67,* and *BUB1B*. These
411 macrophage clusters exhibit distinct gene expression patterns, which may be linked to their distinct

Figure 5 - Genomic regulatory network

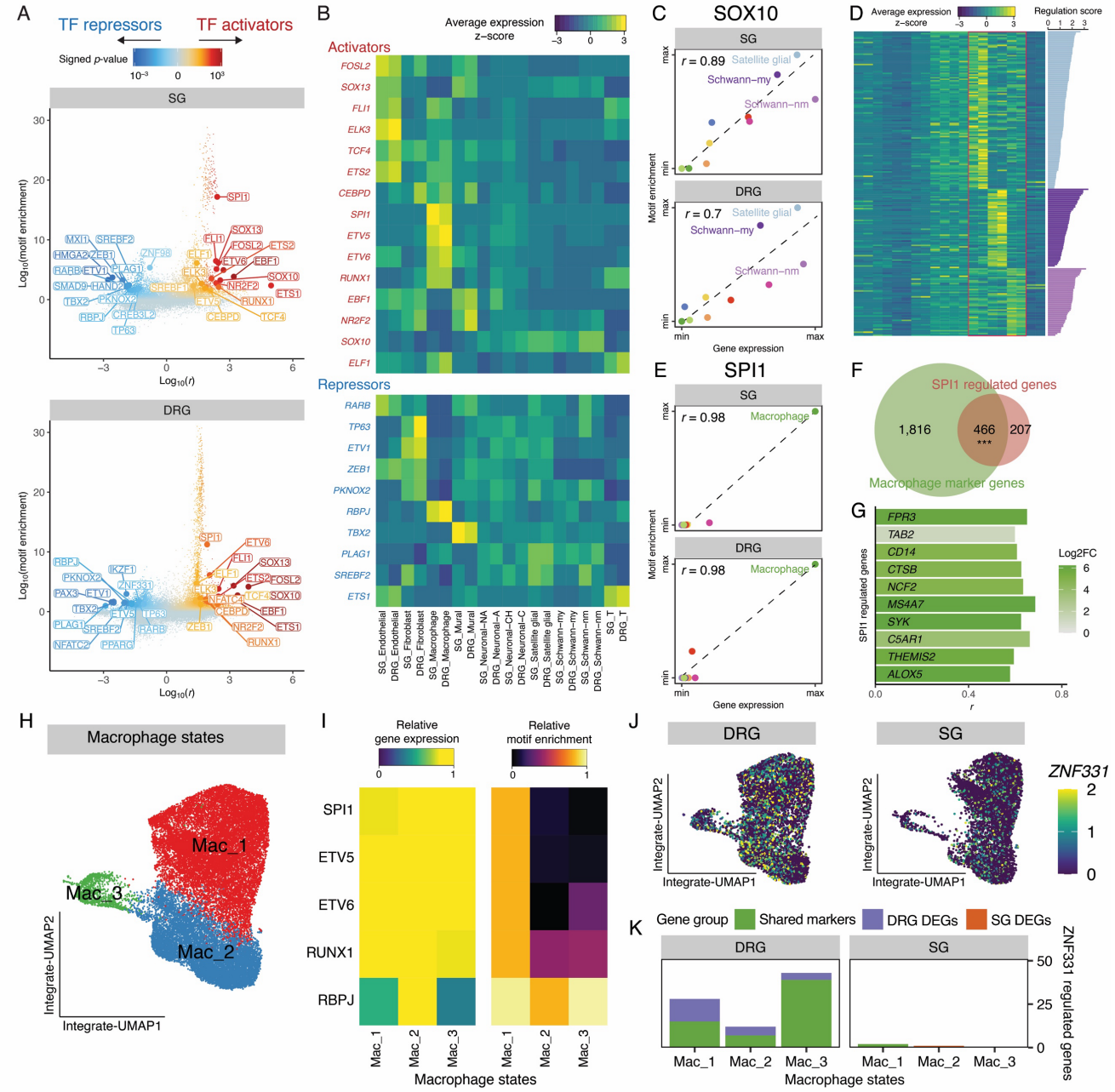

Figure 5. Genomic regulatory networks of human peripheral ganglia

A. Scatter plot showing the TFs enriched in human SG (top) and human DRG. Each dot shows the interaction between one TF and one of its regulated genes. For each TF, the interaction with the highest score is highlighted and labeled. B. Heatmap showing the expression of TF genes in individual SG and DRG cell types based on the snRNA-seq data. C. Scatter plot of the gene expression and motif enrichment of SOX10 in individual SG (top) and DRG (bottom) cell types. Pearson's r and the line of best fit are displayed. D. Heatmap showing the expression of SOX10-regulated marker genes in satellite glial and Schwann cells. The row of the heatmap follows the same order as Figure 5B. Bars show the regulation scores of individual genes by SOX10. E. Scatter plot of the gene expression and motif enrichment of SPI1 in individual SG (top) and DRG (bottom) cell types. Pearson's r and the line of best fit are displayed. F. Overlap between SPI1-regulated genes and macrophage-specific marker genes. Hypergeometric test: p = 6.8E-82 [***]. G. Bar plot showing the top 10 SPI1-regulated genes based on regulation score. Colors indicate the differential expression of genes in macrophages compared to all other cell types. H. Integrative gene expression UMAP showing the subtypes of macrophages from human SG and DRG. I. Heatmaps showing the gene expression (left) and motif enrichment (right) of TFs in macrophage subtypes. J. Integrative gene expression UMAP showing the expression of ZNF331 in SG (right) and DRG (left) macrophages. K. Number of genes predicted to be regulated by ZNF331 in individual DRG and SG macrophage subtypes.

412

413 functions according to the GO analysis (Figure S10B, Table 6). To better understand the potential
414 molecular mechanisms that may govern the macrophage functions, we next investigated the GRNs in
415 those macrophage clusters. While the expression of SPI1, ETV5, ETV6, and RUNX1 is similar across
416 macrophage subtypes in snRNA-seq data, their motifs are more enriched in dividing macrophages than
417 anti- and pro-inflammatory macrophages (Figure 5I), suggesting that, in addition to their roles in
418 macrophage differentiation, those TFs may be especially important for macrophage proliferation and
419 maintenance in human SG and DRG. While not experimentally confirmed, these data promote the
420 hypothesis that there is a self-renewing population of macrophages in peripheral ganglia[16]. The RBPJ
421 gene is expressed 2.7 times higher in anti-inflammatory Mac_1 than in other subtypes, whereas its motif
422 enrichment is much lower in Mac_1 (Figure 5I). RBPJ may act as a negative regulator for controlling
423 macrophage gene expression and polarization of anti- and pro-inflammatory states. Moreover, ZNF331
424 is expressed 1.5 – 2.1 times higher in macrophage subtypes in DRG than SG (Figure 5J), and predicted
425 to regulate 83 genes in DRG, compared to only three genes in SG (Figure 5K, Table 6). Therefore,
426 ZNF331 may be key to drive DRG-specific macrophage gene expression signatures, and functional
427 assessment of ZNF331 control of DRG, but not SG, macrophage inflammatory states will be an important
428 future step.

429 **Cell types implicated in hereditary sensory and autonomic neuropathies**

430 Single-cell atlases are useful for identifying the cell types and genes that may contribute to human
431 diseases [26, 36, 74]. We applied our human PNS atlas to investigate the neurobiological mechanisms
432 of hereditary sensory and autonomic neuropathies (HSAN), a group of genetically and phenotypically
433 heterogeneous, and extremely under-investigated rare disorders primarily affecting the PNS. As
434 pathological human tissues from HSAN patients are extremely rare, we reasoned that our multi-omic
435 atlas of the human peripheral ganglia could provide a new opportunity for localizing and predicting the
436 cell types in which genomic variations drive HSAN pathophysiology by examining the expression of
437 HSAN-associated genes and chromatin accessibility of HSAN-associated GREs in a cell-type-specific
438 fashion.

439 To date, nine types of HSAN have been identified based on the age of onset, clinical features,
440 and genetic inheritance (types I to IX, Figure 6A)[75-79]. The key clinical features of HSAN include
441 sensory dysfunctions (insensitive to pain and temperature, less affected touch sensation and
442 proprioception) and varying degrees of autonomic deficits (e.g., gastrointestinal dysfunction,
443 cardiovascular instability, and anhidrosis or hypohidrosis), with some types also exhibiting motor
444 symptoms[80, 81]. These clinical manifestations suggest that HSAN broadly affects the human PNS, but
445 the effect may vary across different components (sensory, autonomic, motor). Unfortunately, there is no
446 treatment currently available to address the underlying cause and/or prevent the disease progression for
447 the patients. It is thought that mutations in each HSAN type cause disruption in different biological
448 processes in the sensory and autonomic systems (and motor system in some types), but the
449 neurobiological mechanism by which the mutant genes affecting the normal functions of diverse human
450 PNS cell types remains elusive. As the genetic causes of HSAN have been largely identified and mapped
451 to the coding regions in the human genome, we reasoned that our multi-omic atlas of human peripheral
452 ganglia would provide an invaluable opportunity for the examining the diverse cell types in the human
453 PNS that may be affected in HSAN and may provide novel insight into understanding the neurobiological
454 mechanism of HSAN and identifying novel targets for therapeutic interventions.

455 We first examined the expression pattern of HSAN-associated genes in our human SG and DRG
456 atlas, as well as the human spinal cord atlas previously reported[82]. Notably, genes associated with
457 HSAN I subtypes (*SPTLC1*, *SPTLC2*, *ATL1*, *ATL3*, and *DNMT1*) and HSAN II subtypes (*WNK1*,
458 *RETREG1*, *KIF1A*, and *SCN9A*) are expressed in all SG and DRG neuronal cell types, as well as

Figure 6 - Hereditary sensory and autonomic neuropathies

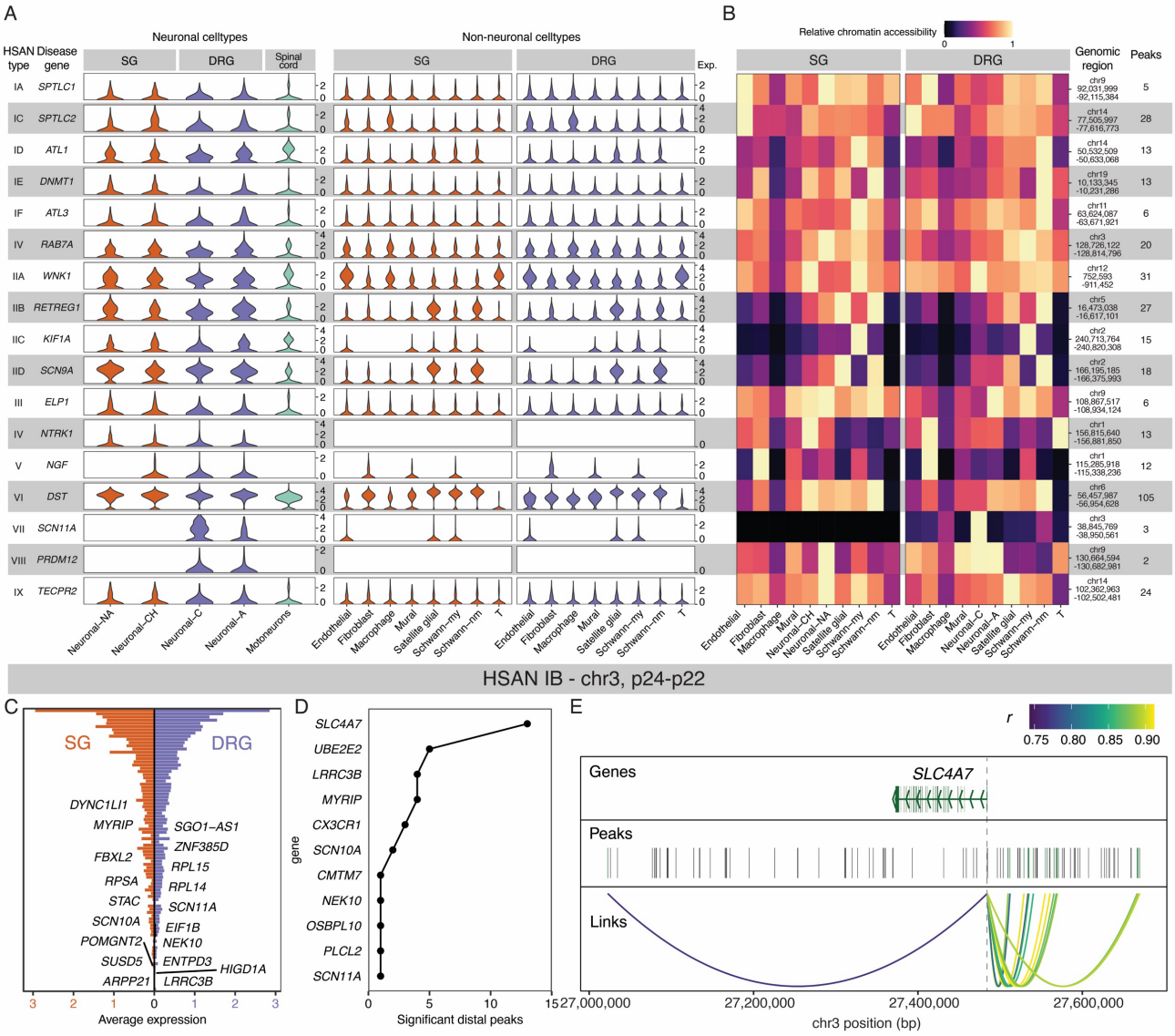

Figure 6. Cell types and genes implicated in hereditary sensory and autonomic neuropathies
A. Violin plots showing the expression of HSAN-associated genes in individual cell types from human SG and DRG, as well as the human spinal cord motoneurons previously reported. B. Heatmap showing the accessibility of genomic loci of HSAN-associated genes in individual human SG and DRG cell types. C. Bar plot showing the genes in the HSAN IB-associated locus that are also expressed in human SG and DRG. Genes that are highly expressed in neuronal cell types (Log2FC > 1, FDR < 0.05 comparing one neuronal cell type to all other nuclei) are highlighted. D. Genes that have significant associations with the distal peaks in the HSAN IB-associated locus. E. The correlation between snATAC-seq peaks with *SLC4A7* in the HSAN IB-associated locus. Distal peaks whose accessibility is highly correlated with *SLC4A7* expression in human SG and DRG cell types are highlighted and linked.

motoneurons (Figure 6A), suggesting the mutant genes may directly affect the normal functions of those neurons, causing the sensory, autonomic, and motor deficits in HSAN I and II patients. HSAN I and II-associated genes are also ubiquitously expressed in most non-neuronal cells from human SG and DRG, prompting the possibility that altered non-neuronal cell function may indirectly contribute to the axonal loss in HSAN I and II. The genomic loci of HSAN I and II-associated genes are broadly accessible in snATAC-seq data in essentially all SG and DRG cell types, corroborating the gene expression pattern from the snRNA-seq data (Figure 6B). Genes associated with HSAN III-VI (*ELP1*, *NTRK1*, *NGF*, and *DST*) and IX (*TECPR2*) are expressed, and their genomic loci are accessible in several neuronal and non-neuronal cell types from human SG and DRG (Figure 6A,B), consistent with the sensory and

autonomic dysregulation reported in the patients. *SCN11A* is important for the perception of pain, and its mutations have been linked to HSAN VII[83, 84]. *SCN11A* is expressed 2.7 times more highly in C-fiber neurons compared to A-fiber neurons in the DRG (Figure 6A), which may explain the inability to experience pain in HSAN VII patients, whereas sensitivity to temperature and touch are less affected. HSAN VII patients also experience mild autonomic dysfunctions, which could be mediated by low levels of *SCN11A* expression in the SG satellite glial cells and Schwann cells (Figure 6A), or the parasympathetic neurons that are not investigated in this study. *RDM12* encodes a transcriptional regulator crucial for the development of nociceptors and pain perception and is associated with HSAN VIII[85, 86]. *PRDM12* is highly expressed in DRG neurons, which is consistent with the congenital insensitivity to pain observed in the patients. However, while *PRDM12* expression is not detected in any of the SG cell types, the chromatin around its locus is accessible in noradrenergic SG neurons. It's currently unknown regarding the possible interaction of PRDM12 with sympathetic neurons during development and how HSAN VIII-associated *PRDM12* mutations contribute to the autonomic deficits reported in the patients.

Potential genes and GREs associated with HSAN IB

Autosomal dominant HSAN IB (also known as HSAN I with cough and gastroesophageal reflux) was reported in the early 2000s, and the genome screen showed linkage to p24-p22 on chromosome 3 (3p24-22), but the exact disease-causing mutations have not yet been identified[87, 88]. We reasoned that a better understanding of the functional genome of the human SG and DRG would help narrow down the possible genetic underpinnings of HSAN IB.

If the mutation(s) occur in the coding region of the genome, the mutant gene(s) expressed in the SG and DRG may contribute to the sensory and autonomic symptoms in HSAN IB patients. Therefore, we first turned to our snRNA-seq data to identify the genes expressed in human peripheral ganglia that may be affected in HSAN IB. We identified 88 genes, out of a total of 304 annotated protein-coding genes in 3p24-22, that are expressed (> 0.1 average counts per cell type) in at least one cell type from human SG and DRG snRNA-seq data (Figure 6C, S11), including 19 genes that are more highly expressed in SG and/or DRG neurons compared to non-neuronal cell types (Log2FC > 1, FDR < 0.05). *EIF1B* (Eukaryotic Translation Initiation Factor 1B), *RPL14*, *RPL15*, and *RPSA* (Ribosomal Proteins L14, L15, and SA, respectively) play critical roles in protein synthesis. *MYRIP* (Myosin VIIA and Rab Interacting Protein) and *DYNC1LI1* (Dynein Cytoplasmic 1 Light Intermediate Chain 1) are important for intracellular and axonal transport. *STAC* (SH3 and Cysteine Rich Domain) has been shown in animal models to regulate the voltage response of calcium channels and the release of neuropeptides, whereas ion channels, *SCN10A* and *SCN11A*, are crucial for the transmission of nociceptive signals. Mutations in those genes may lead to abnormal functions of the sensory and autonomic neurons, which could contribute to the underlying pathology of HSAN IB. In addition, given the important role of glial cells and immune cells in supporting and modulating neuronal functions, abnormal gene functions in those cell types may be a contributor to HSAN IB deficits (Figure S11A).

Moreover, mutations in GREs may alter the regulation and expression of genes, which could be another possible genetic cause of HSAN IB. To study the GRNs regulating gene expression in human SG and DRG cell types that may be associated with HSAN IB, we linked the snATAC-seq peaks in the distal, non-coding region to individual expressed genes in 3p24-22. We found 10 genes with significant association (absolute value of $r > 0.5$) with 36 distal peaks (Figure 6D). For example, *SLC4A7* encodes a sodium bicarbonate cotransporter protein, which plays a crucial role in regulating intracellular pH. *SLC4A7* expression is positively correlated with the accessibility of 12 upstream peaks and one downstream peak (Figure 6E), suggesting that those peaks may contain cis-acting GREs, such as enhancers, that drive the expression of *SLC4A7* when accessible in the genome. In summary, we

515 identified 88 genes expressed in human SG and DRG cell types, as well as 36 putative GREs that
516 function by regulating the expression of those genes. Those genes and putative GREs are functionally
517 relevant to human SG and DRG, and their disruptions may lead to dysfunctions of SG and DRG cell
518 types, which may underlie the HSAN IB pathology.

519

520 **DISCUSSION**

521 In this study, we generated a comprehensive single-cell multi-omic atlas of human peripheral
522 ganglia, including SG and DRG, using snMultiome-seq. By analyzing tissues from multiple donors, we
523 delineated the transcriptional and epigenomic landscapes of various cell types within these peripheral
524 ganglia. This high-resolution atlas reveals shared and distinct molecular features of SG and DRG cell
525 types, providing new insights into the function and regulation of the human PNS. Additionally, we
526 explored the potential implications of these cell types in peripheral neuropathies, specifically focusing
527 on HSAN. This resource offers valuable insights into the physiological functions of these ganglia and
528 their potential alterations in human diseases, which may inspire future investigation of the disease
529 mechanisms and aid the development of novel therapeutic strategies.

530 Our integrated analysis showed a high level of similarity between SG and DRG in terms of
531 cellular composition and cell type-specific gene expression. Both ganglia share several cell types,
532 including neurons, glial cells, endothelial cells, fibroblasts, and immune cells. The composition of each
533 cell type is similar between SG and DRG in our atlas, and the majority of the cell type-specific marker
534 genes are expressed at a similar level between the two ganglia. These cellular and molecular
535 similarities likely reflect the shared developmental origin and the molecular infrastructures required for
536 the basic biological functions of these peripheral ganglia.

537 Despite the overall similarities, distinct transcriptional signatures were observed between SG
538 and DRG cell types, likely reflecting their unique physiological roles. The SG plays a critical role in
539 maintaining homeostasis and mediating stress responses, whereas the DRG is important for relaying
540 the sensory information to the CNS. Their distinct functional roles are exemplified by the molecular
541 profiles of the neurons. we identified two human SG neuronal populations (Figure 1). The noradrenergic
542 neurons express *TH* and *DBH*. While also expressing *TH* and *DBH*, the cholinergic neurons uniquely
543 express *ACHE* and *SLC18A3*. Recent animal studies have suggested specificity in autonomic system
544 response, which is likely mediated by SG neuronal populations. For example, transcriptionally distinct
545 subsets of noradrenergic SG neurons specifically innervate erector muscles and control nipple- and
546 pilo-erection [28], whereas cholinergic SG neurons innervate sweat glands and control sweat secretion
547 [89, 90]. On the other hand, DRG neurons use glutamate to communicate with post-synaptic spinal
548 neurons. A-fiber neurons are large-diameter, fast-conducting, and tend to be preferentially specialized
549 for detecting mechanical stimuli, whereas C-fiber neurons are unmyelinated, slow-conducting, and can
550 detect a broader range of environmental stimuli, including thermal, mechanical, and chemical
551 stimuli[25, 91]. Compared to SG, DRG neurons highly express genes encoding ion channels for
552 nociceptive signal transmission (e.g., *SCN10A* and *SCN11A*) and temperature sensing (*TRPA1* and
553 *TRPM8*, Figure 3). These findings are consistent with previous literature.

554 Our comparative analysis between human and mouse SG datasets also revealed some
555 interesting differences. For example, we found proportionally more abundant myelinated, cholinergic
556 neurons and myelinating Schwann cells, which support the myelinated axons, in our human atlas
557 generated from lumbothoracic paravertebral SG, compared to previous animal studies primarily
558 originated from cervical and thoracic SG. While we did not specifically examine the contribution of
559 different factors (e.g., species difference and/or sympathetic spinal level difference), previous studies

560 have suggested an expansion of cholinergic neurons in human, and perhaps myelinating Schwann
561 cells too. In human SG, cholinergic neurons make up 18-28% of total human SG neurons in a previous
562 study[35], and 33% of total human SG neurons in our atlas. In rodents, cholinergic neurons are
563 estimated to comprise 5% of the neurons in the stellate SG, and as low as 0.1% in paravertebral
564 SG[92, 93]. Moreover, humans cool down body temperature by sweating, whereas other mammals
565 generally dissipate heat in alternative ways, such as panting, increased saliva secretion and blood flow
566 in hairless skin[94]. Sweat glands innervated and regulated by cholinergic SG neurons are more
567 prevalent in humans than in other mammals, which corroborates our observation. Therefore, our
568 findings may reflect the physiological difference of SG innervation and the neurobiological basis of
569 thermoregulation strategies across species.

570 Autonomic and sensory deficits have been reported in various human diseases, suggesting a
571 potential involvement of SG and DRG in those conditions. As the mechanisms by which the dysfunction
572 of human SG and DRG may lead to the autonomic and sensory symptoms in human patients remain
573 unclear, a better understanding of the molecular and cellular diversity of human SG and DRG may help
574 us identify the cell types susceptible to those diseased conditions and explore the potential molecular
575 and cellular mechanisms of human diseases. For example, the accumulation of amyloid plaques, which
576 usually happens when Amyloid Precursor Protein (APP) is erroneously processed, is a hallmark of
577 Alzheimer's disease. Amyloid plaques have been shown to reduce the neurite outgrowth of the
578 sympathetic neurons in a mouse model of Alzheimer's disease[49]. While autonomic dysfunctions are
579 common in dementia patients[52, 53], their underlying neurobiological mechanisms have not been
580 elucidated. Our analysis pinpoints the human SG cell types that express *APP* and may contribute to the
581 amyloid plaque accumulation (Figure 2). In addition, we examined the expression of *CNTN1* and
582 *LAMA2,* genetic causes of specific types of congenital muscular dystrophies, in human SG [50, 51].
583 The expression of the mutant genes in SG cell types likely leads to altered normal SG functions and
584 causes autonomic deficits in human patients, such as gastroesophageal reflux and, in more severe
585 cases, respiratory failure[95]. Moreover, our multi-omic atlas has significant implications for the cell
586 types that may be affected in HSAN. By mapping the expression and regulatory landscapes of HSAN-
587 associated genes, we identified specific cell types likely to be affected in these disorders. Altogether,
588 our human SG and DRG atlas provides insight into the key molecules and cell types associated with
589 human health and diseases, and sheds light on the evolutionary conservation that would aid the future
590 investigation of human diseases using animal models. This atlas can guide future research into the
591 pathophysiology of HSAN and other neuropathies, facilitating the development of targeted therapeutic
592 interventions.

593 Despite the comprehensive analyses in our study, several limitations should be acknowledged.
594 First, the low neuronal proportion in human PNS tissues undermines the profiling of neurons in our
595 atlas, potentially leading to an underestimation of neuronal diversity within the SG and DRG. Future
596 studies with improved representation of neuronal populations (e.g., targeted approaches to enrich
597 neurons and increased sample size) are necessary to capture the full extent of human neuron
598 heterogeneity[25, 34]. In addition, our atlas was generated using human tissues from organ donors,
599 whose demographics may not be enriched for any specific diseases. While our analysis is promising for
600 predicting and narrowing down cell types that may be affected in human diseases, the direct
601 applicability of our findings to pathological conditions is limited and requires further investigation and
602 validation. Future work incorporating tissues from patients or techniques introducing disease-
603 associated mutations to non-pathological human tissues will be crucial for validating and extending our
604 findings.

605

606 **MATERIALS AND METHODS**

607 **Human tissue procurement**

608 Extraction and collection of human SG and DRG tissues were performed as previously
609 described in collaboration with Mid-American Transplant[37], with the following modifications and
610 specifications. Lumbothoracic paravertebral SGs and DRGs (T11 - L5) were surgically removed from
611 postmortem organ donors, within 1 - 3 hours of aortic cross-clamping. Extracted tissues were
612 immediately placed in ice-cold, oxygenated N-methyl-D-glucamine (NMDG)-based artificial
613 cerebrospinal fluid (aCSF; 93 mM NMDG, 2.5 mM KCl, 1.25 mM NaH_2PO_4, 30 mM $NaHCO_3$, 20 mM
614 HEPES, 25 mM glucose, 5 mM ascorbic acid, 2 mM thiourea, 3 mM Na+ pyruvate, 10 mM $MgSO_4$, 0.5
615 mM $CaCl_2$, 12 mM N-acetylcysteine; adjusted to pH 7.3 using NMDG or HCl, and 300 – 310 mOsm
616 using H_2O or sucrose) and transported to the lab. Tissues were inspected, and adjacent tissues were
617 removed. Cleaned tissues were snap-frozen in a liquid nitrogen vapor-based CryoPod Carrier before
618 being transferred to -80 °C for long-term storage. To prepare for sequencing or RNA-FISH, human SG
619 and DRG tissues were embedded in Optimal Cutting Temperature (OCT) compound and sectioned on
620 a cryostat. Several sections were mounted for morphology inspection first, and five to ten 100-µm
621 sections were collected into a nuclease-free 1.5 ml tube for sequencing. 15-µm sections were mounted
622 on glass slides for RNA-FISH. Sections were stored at -80 °C if not used immediately.

623 **Single-nuclei isolation and gradient centrifugation**

624 Nuclear extraction was performed according to a protocol described previously[26]. Tissues
625 were rinsed with PBS to remove OCT and minced with scissors. Minced tissues were resuspended in 1
626 ml of homogenization buffer (0.25 M sucrose, 25 mM KCl, 5 mM $MgCl_2$, 10 mM Tris-HCl, pH 8.0, 5
627 µg/ml actinomycin, 1% BSA, and 0.08 U/ul RNase inhibitor, 0.01% NP40) and transferred to a 2 ml
628 dounce homogenizer on ice. Samples were homogenized for 15 strokes with the loose pestle, followed
629 by 15 additional strokes with the tight pestle. The tissue homogenate was then passed through a 50 µm
630 filter and diluted 1:1 with working solution (50% iodixanol, 25 mM KCl, 5 mM $MgCl_2$, and 10 mM Tris-
631 HCl, pH 8.0). Nuclei were layered onto an iodixanol gradient after homogenization and ultracentrifuged
632 at 8,000 × g for 18 minutes. The gradient centrifugation was used to remove cellular and axonal debris
633 and retain neuronal nuclei from the sample. After ultracentrifugation, nuclei were collected between the
634 30 and 40% iodixanol layers and diluted with resuspension buffer (1 × PBS with 1% BSA and 0.08 U/ul
635 RNase inhibitor). Nuclei were centrifuged at 500 × g for 10 min at 4 °C and resuspended in
636 resuspension buffer with 5 ng/µl of 7-AAD. Nuclei were inspected on a hemocytometer, and
637 concentration was calculated. A step-by-step nuclear extraction protocol is available on protocols.io:
638 https://dx.doi.org/10.17504/protocols.io.5jyl8q4y8l2w/v1.

639 During the preparation of the library hSG-1(Table 1), fluorescence-activated cell/nucleus sorting
640 (FACS) was carried out in an attempt to remove cellular debris. Nuclei were counterstained with 7-AAD
641 and sorted using a 100 mm nozzle and a flow rate of 3 on a BD FACSARIA II into a 1.5 mL
642 microcentrifuge tube containing 15 ml of 1X PBS, 0.04% BSA, and 0.1 U/ul RNase inhibitor. However,
643 only 0.01% of the nuclei from this library were assigned to the neuronal clusters, compared to 2.4 ±
644 0.1% from libraries that were prepared without FACS. We concluded that FACS negatively affected the
645 neuronal coverage and thus prepared the remaining libraries without FACS.

646 **snMultiome-seq**

647 Nuclei were diluted to target 10k nuclei recovery for each library. Diluted nuclei were further
648 processed and prepared for sequencing according to the manufacturer's manuals of 10X Genomics
649 Chromium Single Cell Multiome Assay. Libraries were sequenced on an Illumina NovaSeq X Plus

instrument with 150 cycles each for Read1 and Read2, targeting 50,000 paired reads/nucleus for snRNA-seq libraries and 25,000 paired reads/nucleus for snATAC-seq libraries. Raw sequencing data from individual libraries were processed using 10X Genomics cellranger-arc (V2.0.1) and mapped to human reference genome GRCh38. Data from all eight snMultiome-seq libraries were then merged using cellranger-arc aggr function.

Data processing, quality control, and clustering

The aggregated gene-cell and peak-cell count matrices were loaded and processed using R (V4.4.1) packages Seurat (V5.1.0) and Signac (V1.13.0)[96, 97]. To be included in the analysis, nuclei were required to contain more than 500 unique genes, less than 15,000 UMIs, and fewer than 5% of the counts deriving from mitochondrial genes for the snRNA-seq data, as well as more than 500 but fewer than 100,000 fragments, nucleosomal signal score less than 2, and TSS enrichment score greater than 1 for the snATAC-seq data. In total, there were 61,981 nuclei that met these initial quality control criteria.

Raw gene counts from snRNA-seq were scaled to 10,000 transcripts per nucleus and log-transformed using NormalizeData() function to control the sequencing depth between nuclei. Counts were centered and scaled for each gene using ScaleData() function. Highly variable genes were identified using FindVariableFeatures(), and the top 20 principal components were retrieved with RunPCA() using default parameters. For dimension reduction and visualization, Uniform Manifold Approximation and Projection (UMAP) coordinates for snRNA-seq (RNA-UMAP) were calculated using RunUMAP(). Nuclei clustering was performed using FindClusters() based on the variable features from the top 20 principal components, with the resolution set at 0.6. The marker genes for each cluster were identified using FindAllMarkers(), comparing nuclei in one cluster to all other nuclei. Doublet or low-quality nuclei were identified if they met any of the following criteria: 1). Assigned to a cluster with no significantly enriched marker genes (log2FC > 1, FDR < 0.05); 2). Identified as multiplets using R package DoubletFinder (V2.0.6) with doublet expectation rate at 5%[98]; 3). Assigned to a cluster in which three or more mitochondrial genes were identified among the top 20 marker genes (sorted by log2FC); and 4). Assigned to a cluster in which marker genes for multiple cell types were significantly enriched (log2FC > 1, FDR < 0.05). See the next section for the marker genes used. After iterative rounds of clustering and removal of low-quality clusters, a total of 52,950 high-quality human SG nuclei were included in the final dataset.

Raw peak counts of the high-quality nuclei from snATAC-seq were subsequently processed. Term frequency-inverse document frequency normalization was performed using RunTFIDF() function, and variable peaks were identified using FindTopFeatures(). Dimension reduction was performed with singular value decomposition using RunSVD() function, and UMAP coordinates for snATAC-seq (ATAC-UMAP) were calculated using RunUMAP(). Nuclei clustering was performed using FindClusters() based on the top 20 dimensions with the resolution of 0.6. To control donor variabilities, donor-specific peaks were called on snATAC-seq libraries from each donor using CallPeaks(), a MACS2 wrapper function in Signac. The snATAC-seq library derived from a pool of tissues of three donors was treated as a single donor. Only snATAC-seq peaks, originally identified by cellranger-arc and included in the peak-cell count matrix, that overlap with donor-specific peaks in no fewer than four donors were considered as shared peaks across donors and included in the analysis. ATAC-UMAP coordinates were re-generated by running RunUMAP() on shared peaks.

Cell type annotation

Transcriptional cell types of human SG were assigned to each snRNA-seq cluster based on the canonical marker genes previously reported. Specifically, neuronal clusters are annotated based on the

expression of *SNAP25* and *SYT1* (Figure S1E). Non-neuronal clusters are annotated based on the lack of expression of *SNAP25* and *SYT1*. Cell types were annotated based on the expression of canonical marker genes shown in Figure 1C. To identify subtypes and/or states of macrophages, we performed sub-clustering of the macrophages from human SG and DRG, and annotated the macrophage subtypes using canonical marker genes previously reported (Figure S10A).

Integration with mouse SG snRNA-seq data

To harmonize the SG cell types across species, our human SG snRNA-seq data were integrated with mouse SG snRNA-seq data previously described[4]. Mouse gene names were converted to their human orthologs using the R orthology mapping package Orthology.eg.db (V3.21). The two datasets were then jointly clustered using the clustering approach described above. To facilitate accurate comparative analysis across species, nuclei of different species were then integrated using IntegrateLayers() with CCA integration algorithm. FindClusters() and RunUMAP() were then run on the top 20 components of the integrated CCA space. To establish correspondence between human and mouse SG cell types, which were generated independently by the clustering approach described above, or published previously, the mouse cell type labels were transferred to each human nucleus by assigning the label of the most abundant mouse cell type in each integrated cluster to the human nuclei in the same integrated cluster. Mouse Schwann cells were renamed to myelinating Schwann cells in the analysis, as they express myelinating Schwann cell marker *Ncamp*.

Integration with human DRG snMultiome-seq data

To harmonize the SG cell types between human SG and human DRG, our human SG snMultiome-seq data were integrated with the human DRG snMultiome-seq data described in our companion study [companion study]. The two datasets were first jointly clustered using the clustering approach described above. To facilitate accurate comparative analysis, the two datasets were then integrated using IntegrateLayers() with CCA integration algorithm. FindClusters() and RunUMAP() were then run on the top 20 components of the integrated CCA space. To establish correspondence between human SG and DRG cell types, which were generated independently by the clustering approach described above, or published previously, the human DRG cell type labels were transferred to each human SG nucleus by assigning the label of the most abundant DRG cell type in each integrated cluster to the SG nuclei in the same integrated cluster.

Differential analyses of gene expression and chromatin accessibility

To identify marker genes and peaks that are enriched in each cell type or macrophage subtype, differential expression/accessibility analysis was performed using FindAllMarkers() in Seurat/Signac, comparing nuclei from one cell type to all other nuclei. Genes and peaks with Log2FC > 1 and FDR < 0.05 were reported, unless specified otherwise.

To identify genes and peaks that are differentially expressed/accessible between any two populations (e.g., species-specific genes between human and mouse SG, or ganglion-specific genes between human SG and DRG), pair-wise differential expression/accessibility analysis was performed using FindMarkers() in Seurat/Signac, comparing nuclei of a cell type from one population to nuclei of the same cell type from another population. Genes and peaks with Log2FC > 1 and FDR < 0.05 were reported for the first population, and genes and peaks with Log2FC < (-1) and FDR < 0.05 were reported for the second population.

To identify sex-specific gene expression in each human SG cell type, pseudobulk differential expression analysis was performed to control for technical variations or donor variations across

biological samples of the same sex. Specifically, pseudobulk counts for each cell type and each donor were generated by aggregating counts from nuclei of the same cell type and donor using AggregateExpression() in Seurat. Differential expression analysis was done using DESeq2 (V1.44.0) in R by comparing counts between male and female donors. Genes with Log2FC > 1 and FDR < 0.05 were reported. The snMultiome-seq library derived from a pool of tissues of three donors was excluded from the sex-specific differential analysis. To identify peaks that are differentially accessible between sexes, pair-wise differential accessibility analysis was performed using FindMarkers() in Signac, comparing nuclei of one cell type from male donors to nuclei of the same cell type from female donors. Peaks with Log2FC > 1 and FDR < 0.05 were reported.

Ligand receptor pair analysis

Ligand receptor pair analysis was done using CellChat (V2.1.2)[99]. Human SG and mouse SG snRNA-seq data were analyzed separately. The ligand-receptor interaction databases CellChatDB.mouse and CellChatDB.human were used for mouse and human datasets, respectively. To infer the cell-type-specific communications, we first identified differentially expressed signaling genes in individual cell types using identifyOverExpressedGenes(). Significant interactions between ligands and receptors were identified using identifyOverExpressedInteractions(). Cell-cell communications were calculated using computeCommunProb() and communications present in less than 10 cells were excluded. Finally, cell-cell communications at the significant pathway level were quantified using computeCommunProbPathway().

Gene ontology (GO) analysis

GO analysis was performed using topGO (V2.40.0) in R. Marker genes for each cell type were used as the input gene list. For comparison, the background gene list included all genes that are expressed in at least 5% of the nuclei in the cell type being analyzed. Genes were annotated for their biological process and associated GO terms. Enrichment is defined as the number of annotated genes observed in the input list divided by the number of annotated genes expected from the background list. GO terms with at least 20 annotated genes and enrichment *p*-value < 0.05 were returned.

Functional Inference of Gene Regulation (FigR) analysis

To infer the transcription regulatory networks in human peripheral ganglia, we ran FigR on human SG and DRG snMultiome-seq datasets separately[59]. We first ran runGenePeakcorr() to calculate the Pearson's *r* between the expression of genes in snRNA-seq data and the accessibility of peaks in snATAC-seq data falling within a 50,000bp window around each gene. Genes that are significantly associated ($p < 0.05$) with at least seven peaks were kept. Regulation score for each gene-peak association was calculated using getDORCScores(). To identify GRNs and link TFs to their putative regulated genes, FigR was run with default parameters by calling runFigRGRN(). FigR links TFs to putative regulated genes based on the TF motif enrichment in snATAC-seq peaks and the association of snATAC-seq peaks to genes previously described. TF motif enrichment was computed using chromVAR [100]. The snATAC-seq peak by TF motif overlap annotation matrix was first generated using a list of human TF motif PWMs from the chromVARmotifs package, and used along with the snATAC-seq reads in peak-cell count matrix to generate accessibility Z-scores across all snATAC-seq nuclei. To identify cell-type-specific regulatory mechanisms, we reported GRNs that met the following criteria: 1). The TF gene is differentially expressed in any human SG or DRG cell types (Log2FC>1, FDR<0.05); and 2). The TF motif is significantly enriched in the human SG or DRG dataset, with its average FigR enrichment > 0 across all gene-peak associations. GRNs with their average FigR regulation score > 0.14 across all gene-peak associations are identified as transcription

activators, and TFs with their average FigR regulation score < (-0.07) across all gene-peak associations are identified as transcription repressors.

Analysis of HSAN-associated genes and GREs

Genes and genomic loci associated with HSAN subtypes were retrieved from an online depository (https://neuromuscular.wustl.edu/time/hsn.htm) and previous studies[75, 101]. Expression of HSAN-associated genes in motoneurons was retrieved from snRNA-seq data of the human spinal cord previously described[82]. Ensemble genomic coordinates of HSAN-associated genes were retrieved using biomaRt (V2.60.1). To identify genes that may be affected by HSAN IB, all protein-coding genes in the genomic locus 3p24-22 (chromosome 3, 16,300,000- 43,600,000bp) were retrieved using biomaRt. Genes with average expression > 0.1 in any human SG or DRG cell types are identified as expressed. To study the GREs that may be affected by HSAN IB, we first identified distal snATAC-seq peaks that are present in the non-coding genomic region in 3p24-22. To link distal peaks to putative regulated genes, we calculated Pearson's *r* between the expression of genes expressed in human SG or DRG and the chromatin accessibility of distal peaks falling within a 50,000bp window around each gene. Significantly associated peaks to each gene were called with $r > 0.5$ or < (-0.5).

RNA-FISH

RNA-FISH experiments were performed according to the manufacturer's instructions, using the RNAscope Fluorescent Multiplex kit (Advanced Cell Diagnostics (ACD)) for fresh frozen tissue, as previously described[38]. Briefly, human SG and DRG tissues were frozen in OCT and sectioned into 15 µm sections using a cryostat. RNAScope probes against the following genes were ordered from ACD and multiplexed: Hs-SNAP25-C1 (Cat No. 518851), Hs-PRX-C2 (Cat No. 423911-C2), and Hs-NRXN1-C3 (Cat No. 527151-C3). Probes of *SNAP25*, *NRXN1*, and *PRX* were conjugated with OPAL-520, 570, and 690 for detection and visualization, respectively. Following RNA-FISH, slides were mounted in mounting media containing DAPI. RNA-FISH slides were imaged using a 20X objective on a confocal microscope for analysis, or using a 63X oil immersion objective on selected ROIs for visualization.

FISH quantification

Two SGs and two lumbothoracic paravertebral DRGs from two donors were used for RNA-FISH, one SG and one DRG per donor (Table 1). Two to three non-consecutive sections from each biological sample were stained and used for quantification. For each section, two ROIs around axon regions (axon-enriched ROIs) and two ROIs around neuronal soma regions (neuron-enriched ROIs) were imaged. Five neuron-enriched ROIs and five axon-enriched ROIs per biological sample, or a total of 40 ROIs, were analyzed using cellpose and SCAMPR (Figure S8B)[57, 58]. First, cellpose was used to segment non-neuronal cells based on DAPI signal. Cellpose uses a machine learning algorithm that correctly identifies non-neuronal cells, as more than 98% of manually segmented cells were also segmented by cellpose. However, neurons had very dimmed DAPI staining and were poorly segmented by cellpose. Cell masks with an area > 200 μm^2 or < 30 μm^2 were excluded from the analysis. The resulting cell masks were converted into FIJI-compatible ROIs for downstream processing. In SCAMPR, background subtraction was applied, and image-specific threshold values were calculated per channel to correct the difference in background signal intensity across different images. A gene-cell matrix representing the expression of individual genes was generated based on the percentage of pixels in each cell expressing the gene of interest (the pixel intensity is greater than the image-specific threshold value previously mentioned). *PRX*+ cells were identified as cells with *PRX* expression greater than the 50-percentile across all *PRX*-expressing cells. *NRXN1*+ cells were identified as cells with *NRXN1* expression greater than the 50-percentile across all *NRXN1*-expressing cells. Lipofuscin

autofluorescence was identified as large globular structures that exhibited highly similar fluorescent patterns across all three channels.

Statistical analysis and visualization

Statistical analyses, including the number of samples or cells (n) and *p*-values for each experiment, are noted in the figure legends. Statistics and visualization were performed using R (V4.4.1). Student's t-tests, ANOVA tests, and post-hoc t-tests were performed using the R package stats (V4.2.2). Hypergeometric tests were used to test the significance of the overlap between two groups by calling phyper() function also in the R package stats (V4.2.2). Plots were generated using R packages Seurat (V5.1.0), Signac (V1.13.0), ggplot2 (V3.5.1), gplots (V3.1.3), and CellChat (V2.1.2). Figure 1A was generated using bioRender.

Acknowledgements

First and foremost, we express our deepest gratitude to the organ donors and their families for their invaluable gifts that made this research possible. We thank the past and present members of the Gereau lab for their helpful comments. We thank the Mid-America Transplant for their collaboration in tissue procurement. We thank the Genome Technology Access Center (GTAC) at McDonnell Genome Institute at Washington University School of Medicine for help with snMultiome-seq library construction and sequencing. GTAC is partially supported by NCI Cancer Center Support Grant #P30 CA91842 to the Siteman Cancer Center from the National Center for Research Resources (NCRR), a component of the National Institutes of Health (NIH), and NIH Roadmap for Medical Research.

Funding

This work was supported by the National Institutes of Health (NIH) through the NIH HEAL Initiative under award number U19NS130607 (RWG), part of the PRECISION Human Pain Network.

Author contributions

L.Y., A.C., and R.W.G. designed the sequencing experiments in this study. L.Y. performed the sequencing experiments. L.Y., A.D., K.B., and P.M. performed the sequencing analysis. L.Y., A.D., and R.W.G. designed the RNA-FISH experiments in this study, and L.Y., A.D., and R.T. performed and analyzed the RNA-FISH experiments. A.D., J.D.R., M.P., J.Y., R.S., Z.B., J.M., and J.L. extracted and processed the human SG and DRG tissues. L.Y. wrote the manuscript with feedback from all authors. B.C., G.Z., V.C., A.C., and R.W.G. acquired funding and supervised all aspects of the study.

Competing interests

The authors declared no conflict of interest.

Data and materials availability

Raw and processed data of human SG snMultiome-seq experiments included in this study will be deposited to the NCBI Gene Expression (GEO) SRA with accession number GSEXXX. Processed data from this study is also available on SPARC with DOI: 10.26275/oqxx-si9h. snRNA-seq data from mouse SG previously reported are available on GEO: GSE175421[4]. snMultiome-seq data from human DRG reported in our companion study are available on GEO: GSEXXXX and SPARC with DOI: XXX[companion study].

REFERENCES

1. Marmigere, F. and P. Ernfors, *Specification and connectivity of neuronal subtypes in the sensory lineage.* Nat Rev Neurosci, 2007. **8**(2): p. 114-27.
2. Goldstein, D.S., *Differential responses of components of the autonomic nervous system.* Handb Clin Neurol, 2013. **117**: p. 13-22.
3. Sapio, M.R., et al., *Comparative Analysis of Dorsal Root, Nodose and Sympathetic Ganglia for the Development of New Analgesics.* Front Neurosci, 2020. **14**: p. 615362.
4. Mapps, A.A., et al., *Diversity of satellite glia in sympathetic and sensory ganglia.* Cell Rep, 2022. **38**(5): p. 110328.
5. Scott-Solomon, E., E. Boehm, and R. Kuruvilla, *The sympathetic nervous system in development and disease.* Nat Rev Neurosci, 2021. **22**(11): p. 685-702.
6. Hodge, C.J., *Sensory Neurons: Diversity, Development, and Plasticity.* Neurosurgery, 1994. **34**(5): p. 939.
7. Julius, D., *TRP channels and pain.* Annu Rev Cell Dev Biol, 2013. **29**: p. 355-84.
8. Abraira, V.E. and D.D. Ginty, *The sensory neurons of touch.* Neuron, 2013. **79**(4): p. 618-39.
9. Pannese, E., *The satellite cells of the sensory ganglia.* Adv Anat Embryol Cell Biol, 1981. **65**: p. 1-111.
10. Hanani, M. and D.C. Spray, *Emerging importance of satellite glia in nervous system function and dysfunction.* Nat Rev Neurosci, 2020. **21**(9): p. 485-498.
11. Jessen, K.R. and R. Mirsky, *The origin and development of glial cells in peripheral nerves.* Nat Rev Neurosci, 2005. **6**(9): p. 671-82.
12. Monk, K.R., M.L. Feltri, and C. Taveggia, *New insights on Schwann cell development.* Glia, 2015. **63**(8): p. 1376-93.
13. Sapio, M.R., et al., *Analgesic candidate adenosine A 3 receptors are expressed by perineuronal peripheral macrophages in human dorsal root ganglion and spinal cord microglia.* Pain, 2024. **165**(10): p. 2323-2343.
14. Avraham, O., et al., *Profiling the molecular signature of satellite glial cells at the single cell level reveals high similarities between rodents and humans.* Pain, 2022.
15. Guimaraes, R.M., et al., *Neuron-associated macrophage proliferation in the sensory ganglia is associated with peripheral nerve injury-induced neuropathic pain involving CX3CR1 signaling.* Elife, 2023. **12**.
16. Feng, R., et al., *Self-renewing macrophages in dorsal root ganglia contribute to promote nerve regeneration.* Proc Natl Acad Sci U S A, 2023. **120**(7): p. e2215906120.
17. Wang, P.L., et al., *Peripheral nerve resident macrophages share tissue-specific programming and features of activated microglia.* Nat Commun, 2020. **11**(1): p. 2552.
18. Zigmond, R.E. and F.D. Echevarria, *Macrophage biology in the peripheral nervous system after injury.* Prog Neurobiol, 2019. **173**: p. 102-121.
19. Jain, A., et al., *Nociceptor-immune interactomes reveal insult-specific immune signatures of pain.* Nat Immunol, 2024. **25**(7): p. 1296-1305.
20. Hakim, S., et al., *Macrophages protect against sensory axon loss in peripheral neuropathy.* Nature, 2025. **640**(8057): p. 212-220.
21. Wang, J.G., et al., *Local inflammation in rat dorsal root ganglion alters excitability and ion currents in small-diameter sensory neurons.* Anesthesiology, 2007. **107**(2): p. 322-32.
22. Yu, X., et al., *Dorsal root ganglion macrophages contribute to both the initiation and persistence of neuropathic pain.* Nat Commun, 2020. **11**(1): p. 264.
23. Choi, J., et al., *Diverse cell types establish a pathogenic immune environment in peripheral neuropathy.* J Neuroinflammation, 2025. **22**(1): p. 138.
24. Zhao, L., et al., *Single-cell profiling of cellular changes in the somatic peripheral nerves following nerve injury.* Front Pharmacol, 2024. **15**: p. 1448253.
25. Bhuiyan, S.A., et al., *Harmonized cross-species cell atlases of trigeminal and dorsal root ganglia.* Sci Adv, 2024. **10**(25): p. eadj9173.
26. Yang, L., et al., *Human and mouse trigeminal ganglia cell atlas implicates multiple cell types in migraine.* Neuron, 2022. **110**(11): p. 1806-1821 e8.
27. Renthal, W., et al., *Transcriptional reprogramming of distinct peripheral sensory neuron subtypes after axonal injury.* Neuron, 2020. **108**(1): p. 128-144. e9.
28. Furlan, A., et al., *Visceral motor neuron diversity delineates a cellular basis for nipple- and pilo-erection muscle control.* Nat Neurosci, 2016. **19**(10): p. 1331-40.
29. Usoskin, D., et al., *Unbiased classification of sensory neuron types by large-scale single-cell RNA sequencing*, in *Nature Neuroscience*. 2015, Nature Publishing Group. p. 145-153.
30. Elbaz, B., et al., *Sensory neurons display cell-type-specific vulnerability to loss of neuron-glia interactions.* Cell reports, 2022. **40**(3): p. 111130.
31. Sjoholm, L.K., et al., *Evaluation of Post-Mortem Effects on Global Brain DNA Methylation and Hydroxymethylation.* Basic Clin Pharmacol Toxicol, 2018. **122**(2): p. 208-213.

32. Olney, K.C., et al., *Postmortem Interval Leads to Loss of Disease-Specific Signatures in Brain Tissue.* eNeuro, 2025. **12**(3).
33. Huang, H.S., et al., *Chromatin immunoprecipitation in postmortem brain.* J Neurosci Methods, 2006. **156**(1-2): p. 284-92.
34. Yu, H., et al., *Leveraging deep single-soma RNA sequencing to explore the neural basis of human somatosensation.* Nat Neurosci, 2024. **27**(12): p. 2326-2340.
35. Moreno, M.M., et al., *Spatial transcriptomic profiling of human paravertebral sympathetic chain ganglia reveals diabetes-induced neuroplasticity.* bioRxiv, 2025: p. 2025.06.24.661373.
36. Arokiaraj, C.M., et al., *Spatial, transcriptomic, and epigenomic analyses link dorsal horn neurons to chronic pain genetic predisposition.* Cell Rep, 2024. **43**(11): p. 114876.
37. Valtcheva, M.V., et al., *Surgical extraction of human dorsal root ganglia from organ donors and preparation of primary sensory neuron cultures.* Nat Protoc, 2016. **11**(10): p. 1877-88.
38. Yi, J., et al., *Human sensory neurons exhibit cell-type-specific, pain-associated differences in intrinsic excitability and expression of SCN9A and SCN10A.* bioRxiv, 2025.
39. Yi, J., et al., *Bradykinin receptor expression and bradykinin-mediated sensitization of human sensory neurons.* Pain, 2024. **165**(1): p. 202-215.
40. Mapps, A.A., et al., *Satellite glia modulate sympathetic neuron survival, activity, and autonomic function.* Elife, 2022. **11**.
41. Lu, J., et al., *New Insights on the Role of Satellite Glial Cells.* Stem Cell Rev Rep, 2023. **19**(2): p. 358-367.
42. Qi, F., *Sex differences in autonomic function*, in *Primer on the Autonomic Nervous System (Fourth Edition)*, K.B. Italo Biaggioni, Gregory Fink, Jens Jordan, Phillip A. Low, Julian F.R. Paton, Editor. 2023, Academic Press. p. 267-272.
43. Lambert, E., et al., *Gender differences in sympathetic nervous activity: influence of body mass and blood pressure.* J Hypertens, 2007. **25**(7): p. 1411-9.
44. Klassen, S.A., M.J. Joyner, and S.E. Baker, *The impact of ageing and sex on sympathetic neurocirculatory regulation.* Semin Cell Dev Biol, 2021. **116**: p. 72-81.
45. Nahvi, R.J. and E.L. Sabban, *Sex Differences in the Neuropeptide Y System and Implications for Stress Related Disorders.* Biomolecules, 2020. **10**(9).
46. Caldwell, J.H., et al., *Roles of the amyloid precursor protein family in the peripheral nervous system.* Mechanisms of Development, 2013. **130**(6): p. 433-446.
47. Weyer, S.W., et al., *APP and APLP2 are essential at PNS and CNS synapses for transmission, spatial learning and LTP.* EMBO J, 2011. **30**(11): p. 2266-80.
48. Gnanapavan, S. and G. Giovannoni, *Neural cell adhesion molecules in brain plasticity and disease.* Multiple Sclerosis and Related Disorders, 2013. **2**(1): p. 13-20.
49. Bengoechea, T.G., et al., *p75 reduces β-amyloid-induced sympathetic innervation deficits in an Alzheimer's disease mouse model.* Proceedings of the National Academy of Sciences, 2009. **106**(19): p. 7870-7875.
50. Barraza-Flores, P., et al., *Laminin and Integrin in LAMA2-Related Congenital Muscular Dystrophy: From Disease to Therapeutics.* Front Mol Neurosci, 2020. **13**: p. 1.
51. Compton, A.G., et al., *Mutations in contactin-1, a neural adhesion and neuromuscular junction protein, cause a familial form of lethal congenital myopathy.* Am J Hum Genet, 2008. **83**(6): p. 714-24.
52. Dalise, A.M., et al., *Autonomic Nervous System and Cognitive Impairment in Older Patients: Evidence From Long-Term Heart Rate Variability in Real-Life Setting.* Frontiers in Aging Neuroscience, 2020. **Volume 12 - 2020**.
53. Allan, L.M., *Diagnosis and Management of Autonomic Dysfunction in Dementia Syndromes.* Curr Treat Options Neurol, 2019. **21**(8): p. 38.
54. Gutierrez, S., et al., *Tachykinins modulate nociceptive responsiveness and sensitization: In vivo electrical characterization of primary sensory neurons in tachykinin knockout (Tac1 KO) mice.* Mol Pain, 2019. **15**: p. 1744806919845750.
55. Cao, Y.Q., et al., *Primary afferent tachykinins are required to experience moderate to intense pain.* Nature, 1998. **392**(6674): p. 390-4.
56. Hanani, M., *Satellite glial cells in sympathetic and parasympathetic ganglia: in search of function.* Brain Res Rev, 2010. **64**(2): p. 304-27.
57. Pachitariu, M., M. Rariden, and C. Stringer, *Cellpose-SAM: superhuman generalization for cellular segmentation.* bioRxiv, 2025: p. 2025.04.28.651001.
58. Ali Marandi Ghoddousi, R., et al., *SCAMPR, a single-cell automated multiplex pipeline for RNA quantification and spatial mapping.* Cell Rep Methods, 2022. **2**(10): p. 100316.
59. Kartha, V.K., et al., *Functional inference of gene regulation using single-cell multi-omics.* Cell Genom, 2022. **2**(9).
60. Britsch, S., et al., *The transcription factor Sox10 is a key regulator of peripheral glial development.* Genes Dev, 2001. **15**(1): p. 66-78.
61. Bremer, M., et al., *Sox10 is required for Schwann-cell homeostasis and myelin maintenance in the adult peripheral nerve.* Glia, 2011. **59**(7): p. 1022-32.

987 62. Pingault, V., et al., *SOX10: 20 years of phenotypic plurality and current understanding of its developmental*
988 *function.* J Med Genet, 2022. **59**(2): p. 105-114.
989 63. Fang, Y., et al., *The role of a key transcription factor PU.1 in autoimmune diseases.* Front Immunol, 2022.
990 **13**: p. 1001201.
991 64. DeKoter, R.P., J.C. Walsh, and H. Singh, *PU.1 regulates both cytokine-dependent proliferation and*
992 *differentiation of granulocyte/macrophage progenitors.* EMBO J, 1998. **17**(15): p. 4456-68.
993 65. Li, G., W. Hao, and W. Hu, *Transcription factor PU.1 and immune cell differentiation (Review).* Int J Mol
994 Med, 2020. **46**(6): p. 1943-1950.
995 66. Morikawa, Y., et al., *The basic helix-loop-helix factor Hand 2 regulates autonomic nervous system*
996 *development.* Dev Dyn, 2005. **234**(3): p. 613-21.
997 67. Morikawa, Y., et al., *Hand2 determines the noradrenergic phenotype in the mouse sympathetic nervous*
998 *system.* Dev Biol, 2007. **307**(1): p. 114-26.
999 68. Monsoro-Burq, A.H., *PAX transcription factors in neural crest development.* Semin Cell Dev Biol, 2015. **44**:
1000 p. 87-96.
1001 69. Koblar, S.A., et al., *Pax-3 regulates neurogenesis in neural crest-derived precursor cells.* J Neurosci Res,
1002 1999. **56**(5): p. 518-30.
1003 70. Chen, O., C.R. Donnelly, and R.R. Ji, *Regulation of pain by neuro-immune interactions between*
1004 *macrophages and nociceptor sensory neurons.* Curr Opin Neurobiol, 2020. **62**: p. 17-25.
1005 71. Martinez-Sanchez, N., et al., *The sympathetic nervous system in the 21st century: Neuroimmune*
1006 *interactions in metabolic homeostasis and obesity.* Neuron, 2022. **110**(21): p. 3597-3626.
1007 72. Klein Wolterink, R.G.J., et al., *Neuroimmune Interactions in Peripheral Organs.* Annu Rev Neurosci, 2022.
1008 **45**: p. 339-360.
1009 73. Lund, H., et al., *CD163+ macrophages monitor enhanced permeability at the blood-dorsal root ganglion*
1010 *barrier.* J Exp Med, 2024. **221**(2).
1011 74. Kupari, J., et al., *Single cell transcriptomics of primate sensory neurons identifies cell types associated with*
1012 *chronic pain*, in *Nature Communications*. 2021, Nature Research. p. 1-15.
1013 75. Dyck, P.J., Peter Kynaston Thomas, and Edward Howard Lambert, *Peripheral neuropathy*. Vol. 2. 1975:
1014 Saunders.
1015 76. Edvardson, S., et al., *Hereditary sensory autonomic neuropathy caused by a mutation in dystonin.* Ann
1016 Neurol, 2012. **71**(4): p. 569-72.
1017 77. Leipold, E., et al., *A de novo gain-of-function mutation in SCN11A causes loss of pain perception.* Nat Genet,
1018 2013. **45**(11): p. 1399-404.
1019 78. Chen, Y.C., et al., *Transcriptional regulator PRDM12 is essential for human pain perception.* Nat Genet,
1020 2015. **47**(7): p. 803-8.
1021 79. Heimer, G., et al., *TECPR2 mutations cause a new subtype of familial dysautonomia like hereditary sensory*
1022 *autonomic neuropathy with intellectual disability.* Eur J Paediatr Neurol, 2016. **20**(1): p. 69-79.
1023 80. Lischka, A., et al., *Genetic pain loss disorders.* Nat Rev Dis Primers, 2022. **8**(1): p. 41.
1024 81. Renthal, W., *Pain Genetics*, in *Rosenberg's Molecular and Genetic Basis of Neurological and Psychiatric*
1025 *Disease (Fifth Edition)*, J.M.P. Roger N. Rosenberg, Editor. 2015, Academic Press.
1026 82. Yadav, A., et al., *A cellular taxonomy of the adult human spinal cord.* Neuron, 2023. **111**(3): p. 328-344 e7.
1027 83. Leipold, E., et al., *A de novo gain-of-function mutation in SCN11A causes loss of pain perception.* Nat Genet,
1028 2013. **45**(11): p. 1399-404.
1029 84. Salvatierra, J., et al., *A disease mutation reveals a role for NaV1.9 in acute itch.* J Clin Invest, 2018. **128**(12):
1030 p. 5434-5447.
1031 85. Chen, Y.C., et al., *Transcriptional regulator PRDM12 is essential for human pain perception.* Nat Genet,
1032 2015. **47**(7): p. 803-8.
1033 86. Zhang, S., et al., *Clinical features for diagnosis and management of patients with PRDM12 congenital*
1034 *insensitivity to pain.* J Med Genet, 2016. **53**(8): p. 533-5.
1035 87. Kok, C., et al., *A locus for hereditary sensory neuropathy with cough and gastroesophageal reflux on*
1036 *chromosome 3p22-p24.* Am J Hum Genet, 2003. **73**(3): p. 632-7.
1037 88. Spring, P.J., et al., *Autosomal dominant hereditary sensory neuropathy with chronic cough and gastro-*
1038 *oesophageal reflux: clinical features in two families linked to chromosome 3p22-p24.* Brain, 2005. **128**(Pt 12): p.
1039 2797-810.
1040 89. Schotzinger, R., X. Yin, and S. Landis, *Target determination of neurotransmitter phenotype in sympathetic*
1041 *neurons.* J Neurobiol, 1994. **25**(6): p. 620-39.
1042 90. Stevens, L.M. and S.C. Landis, *Development and properties of the secretory response in rat sweat glands:*
1043 *relationship to the induction of cholinergic function in sweat gland innervation.* Dev Biol, 1987. **123**(1): p. 179-90.
1044 91. Kupari, J. and P. Ernfors, *Molecular taxonomy of nociceptors and pruriceptors.* Pain, 2023. **164**(6): p. 1245-
1045 1257.

1046 92. Schafer, M.K., L.E. Eiden, and E. Weihe, *Cholinergic neurons and terminal fields revealed by*
1047 *immunohistochemistry for the vesicular acetylcholine transporter. II. The peripheral nervous system.* Neuroscience,
1048 1998. **84**(2): p. 361-76.
1049 93. Morales, M.A., et al., *Localization of choline acetyltransferase in rat peripheral sympathetic neurons and its*
1050 *coexistence with nitric oxide synthase and neuropeptides.* Proc Natl Acad Sci U S A, 1995. **92**(25): p. 11819-23.
1051 94. Cui, C.Y. and D. Schlessinger, *Eccrine sweat gland development and sweat secretion.* Exp Dermatol, 2015.
1052 **24**(9): p. 644-50.
1053 95. Oliveira, J., et al., *LAMA2 gene mutation update: Toward a more comprehensive picture of the laminin-*
1054 *alpha2 variome and its related phenotypes.* Hum Mutat, 2018. **39**(10): p. 1314-1337.
1055 96. Hao, Y., et al., *Dictionary learning for integrative, multimodal and scalable single-cell analysis.* Nat
1056 Biotechnol, 2024. **42**(2): p. 293-304.
1057 97. Stuart, T., et al., *Single-cell chromatin state analysis with Signac.* Nat Methods, 2021. **18**(11): p. 1333-1341.
1058 98. McGinnis, C.S., L.M. Murrow, and Z.J. Gartner, *DoubletFinder: Doublet Detection in Single-Cell RNA*
1059 *Sequencing Data Using Artificial Nearest Neighbors.* Cell Syst, 2019. **8**(4): p. 329-337 e4.
1060 99. Jin, S., et al., *Inference and analysis of cell-cell communication using CellChat.* Nat Commun, 2021. **12**(1):
1061 p. 1088.
1062 100. Schep, A.N., et al., *chromVAR: inferring transcription-factor-associated accessibility from single-cell*
1063 *epigenomic data.* Nat Methods, 2017. **14**(10): p. 975-978.
1064 101. Lischka, A., et al., *Genetic pain loss disorders.* Nat Rev Dis Primers, 2022. **8**(1): p. 41.

1065

Figure S1 - Quality control metrics

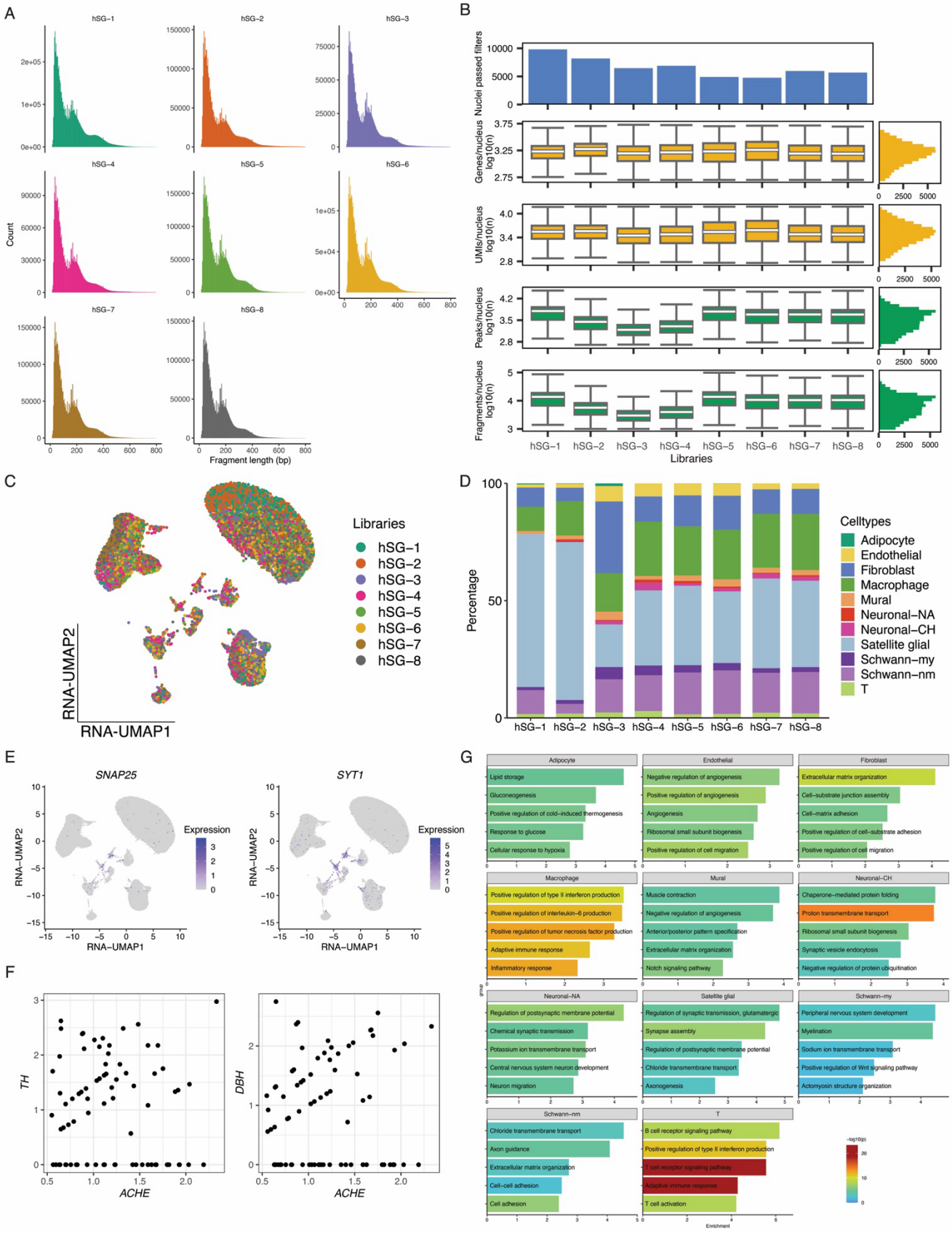

Figure S1.

A. Length distribution of snATAC-seq fragments mapped to the first 1M base pairs in Chromosome one in nuclei grouped by transcriptional cell types. **B**. Quality control metrics of snMultiome-seq libraries. Top row displays number of nuclei passed quality control. Second and third rows display box plots of number of genes and UMIs per nucleus (log10 transformed) in snRNA-seq libraries. Bottom two rows display the number of peaks and transposase-sensitive DNA fragments per nucleus in snATAC-seq libraries. Boxes indicate quartiles and whiskers are 1.5-times the interquartile range (Q1-Q3). The median is a white line inside each box. The distribution is aggregated across all samples and displayed on the horizontal histogram. **C**. Gene expression UMAP of 2,000 downsampled nuclei per library. Nuclei were colored by libraries. **D**. Composition of transcriptional cell types in each snMultiome-seq library. **E**. Gene expression UMAP showing the expression of neuronal marker genes *SNAP25* (top) and *SYT1* (bottom). **F**. Scatter plots shpwing the co-expression of noradrenergic neuronal marker *ACHE* with cholinergic neuronal markers *TH* (left) and *DBH* (right) in individual nuclei from the noradrenergic neuron cluster. **G**. Bar plot showing the top five significant gene ontology terms per cell type. Color denotes the p-values associated with each term.

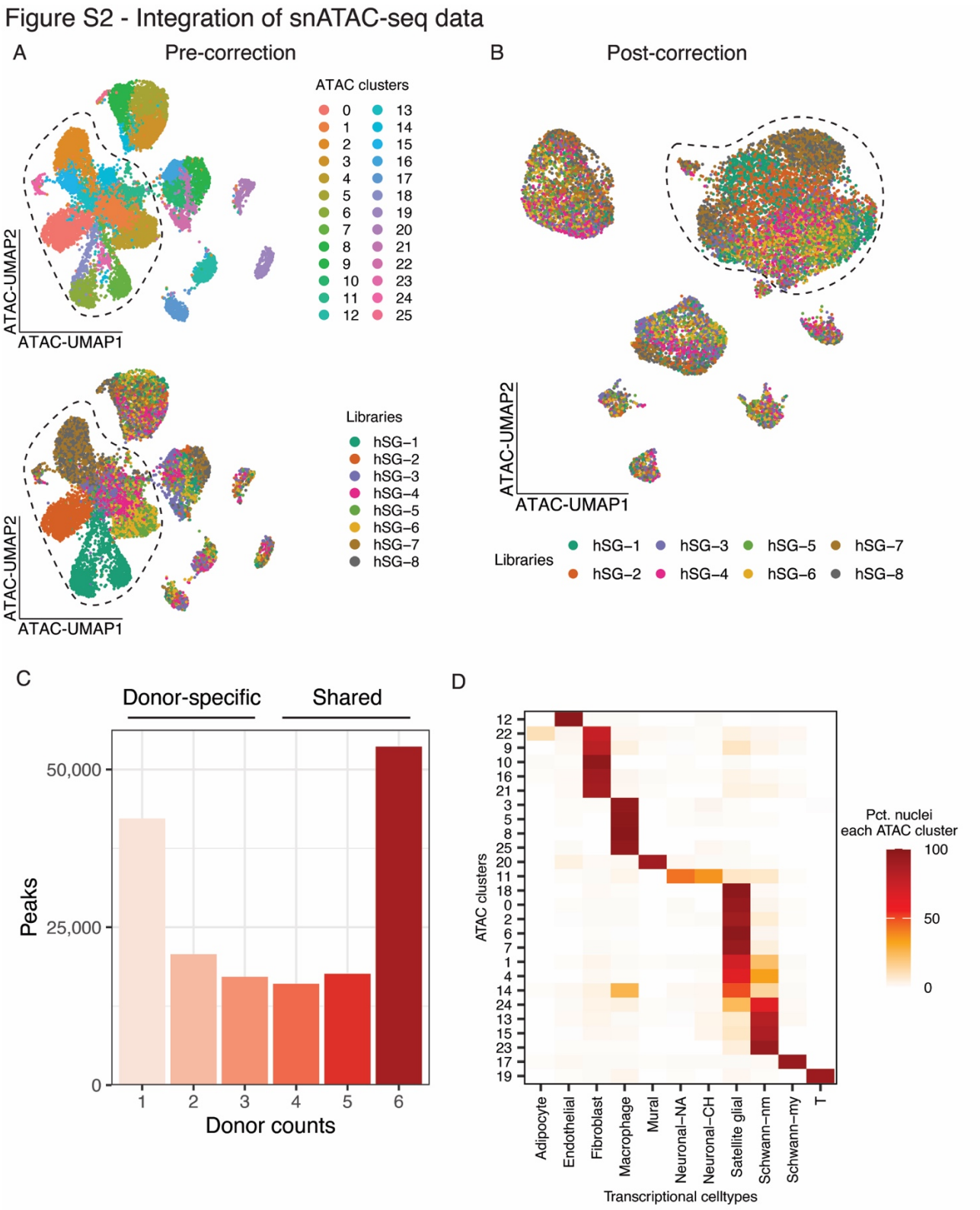

Figure S2.

A. Chromatin accessibility UMAP of 2,000 downsampled nuclei per library based on all peaks. Nuclei were colored by snATAC-seq clusters (top) or libraries (bottom). The dotted line highlights satellite glial cell clusters. **B**. Chromatin accessibility UMAP of 2,000 downsampled nuclei per library based on shared peaks across donors. Nuclei were colored by libraries. The dotted line highlights satellite glial cell clusters shown in S2A. **C**. Distribution of snATAC-seq peaks based on their accessibility across

donors. Peaks are called per donor using MACS2, and snATAC-seq peaks that are present in less than four donors are classified as ‘Donor-specific’, and peaks present in at least four donors are classified as ‘shared’ and subsequently used in the snATAC-seq clustering in S2B. **D**. Overlap of human TG cell types between the snATAC-seq clustering and the cell type classifications assigned by snRNA-seq clustering. Plot displays fraction of nuclei within each snATAC-seq cluster that is assigned to each transcriptional cell type.

Figure S3 - Sex-specific transcriptional and epigenomic features

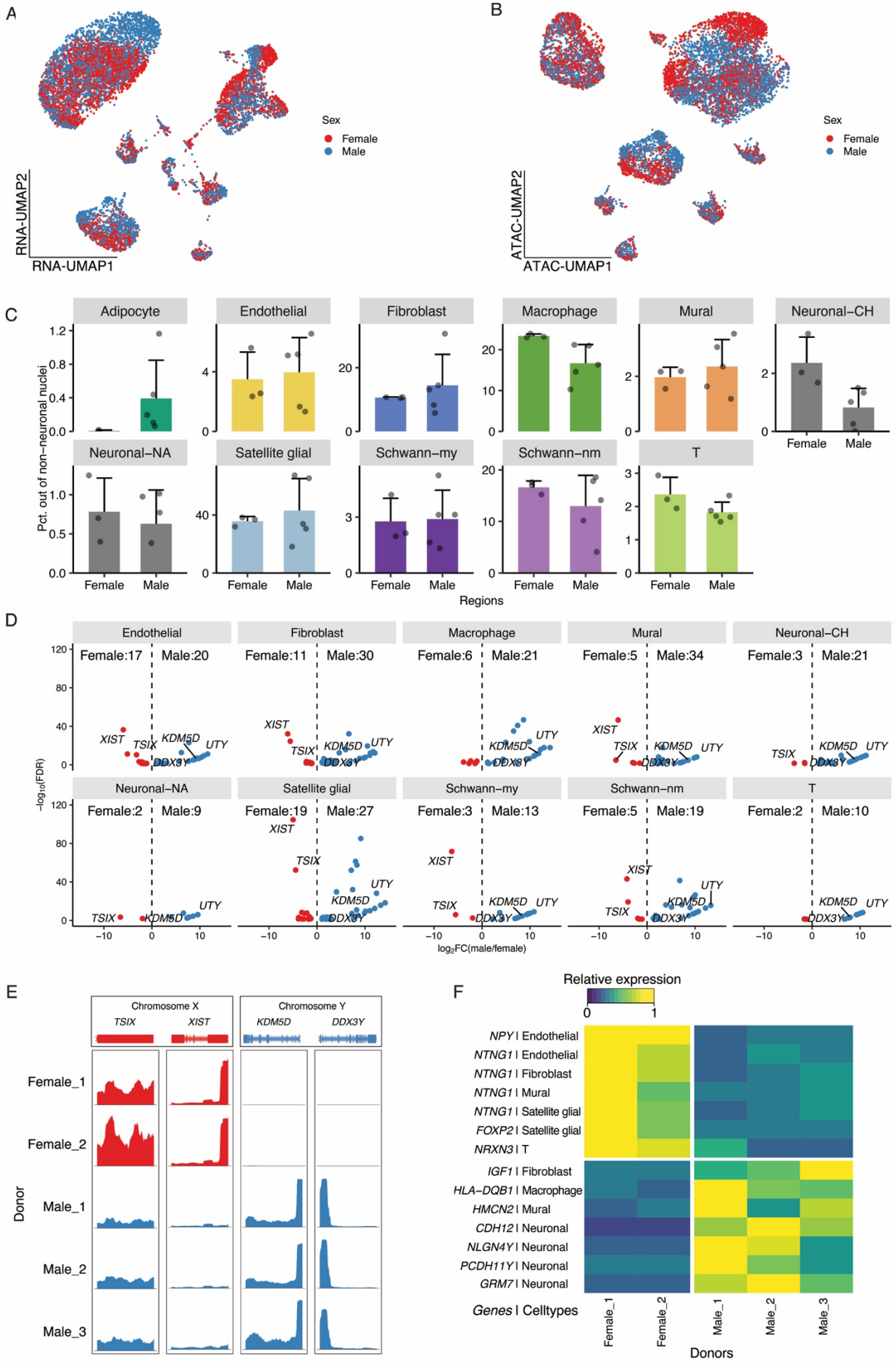

Figure S3.

A and **B**. Gene expression (A) and chromatin accessibility (B) UMAP of 5,000 downsampled nuclei per sex. Nuclei were colored by donors' sex. **C**. Bar plot showing the composition of cell types in SG libraries between sex. ($p = 0.99$ for adipocytes, $p = 0.89$ for endothelial cells, $p = 0.71$ for fibroblasts, $p = 0.03$ for macrophages, $p = 0.98$ for mural cells, $p = 0.99$ for Neuronal-NA, $p = 0.71$ for Neuronal-CH, $p = 0.9$ for satellite glial cells, $p = 0.99$ for schwann-my, $p = 0.99$ for schwann-nm, and $p = 1$ for T cells. Bonferroni-corrected student t-tests [*$p = 0.0045$, **$p = 0.0009$, ***$p = 0.00009$]. **D.** Volcano plots showing the differentially expressed genes (Log2FC > 1 for male and Log2FC < (-1) for female, FDR < 0.05) in individual cell types between nuclei from male donors and female donors. Known sex-specific genes are labeled. Cell types with less than 50 nuclei per sex were excluded form the analysis. **E**. Coverage plot showing the accessibility around genomic loci of known sex-specific genes in snATAC-seq libraries from individual donors. The chromatin accessibility is displayed as the relative frequency of sequenced DNA fragments for each donor, grouped by 50 bins per displayed genomic region. The frequency is normalized by the maximal frequency per genomic region. **F**. Heatmap showing the relative expression of selected sex-specific genes in a given cell type. Color denotes relative expression of a gene in the cell type specified in the row name across all donors (calculated as the mean expression of a gene relative to the highest mean expression of that gene across all donors).

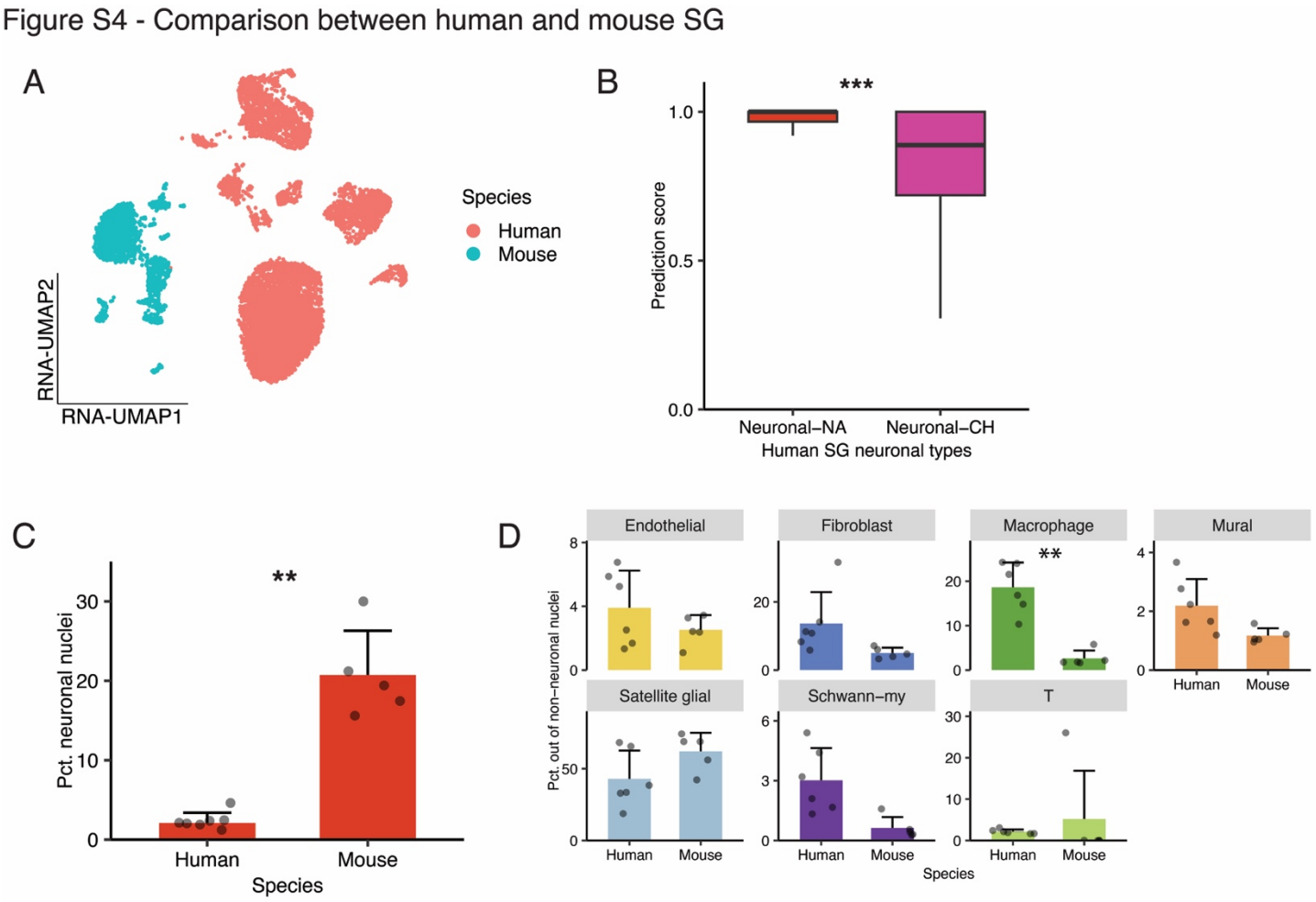

Figure S4.

A. Gene expression UMAP of human and mouse SG when clustering together without integration. 5,000 nuclei are randomly sampled per species. Nuclei are colored by species. **B**. Box plot showing the prediction score when anchoring human neuronal nuclei of two neuronal cell types to the mouse neuronal nuclei that are mostly noradrenergic. (p = 2.2e-16 [***], student t-test). **C**. Bar plot showing the percentage of nuclei that are neuronal in human and mouse SG snRNA-seq libraries. (p = 0.0014 [**], student t-test). **D**. Bar plot showing the composition of non-neuronal cell types among all non-neuronal nuclei in human and mouse SG libraries. (p = 0.22 for endothelial cells, p = 0.07 for fibroblasts, p = 0.0005 [**] for macrophages, p = 0.04 for mural cells, p = 0.048 for satellite glial cells, p = 0.01 for schwann-my, and p = 0.59 for T cells. Bonferroni-corrected student t-tests comparing percentages of a given cell type in human libraries to those in mouse libraries [*p = 0.007, **p = 0.0014, ***p = 0.00014].

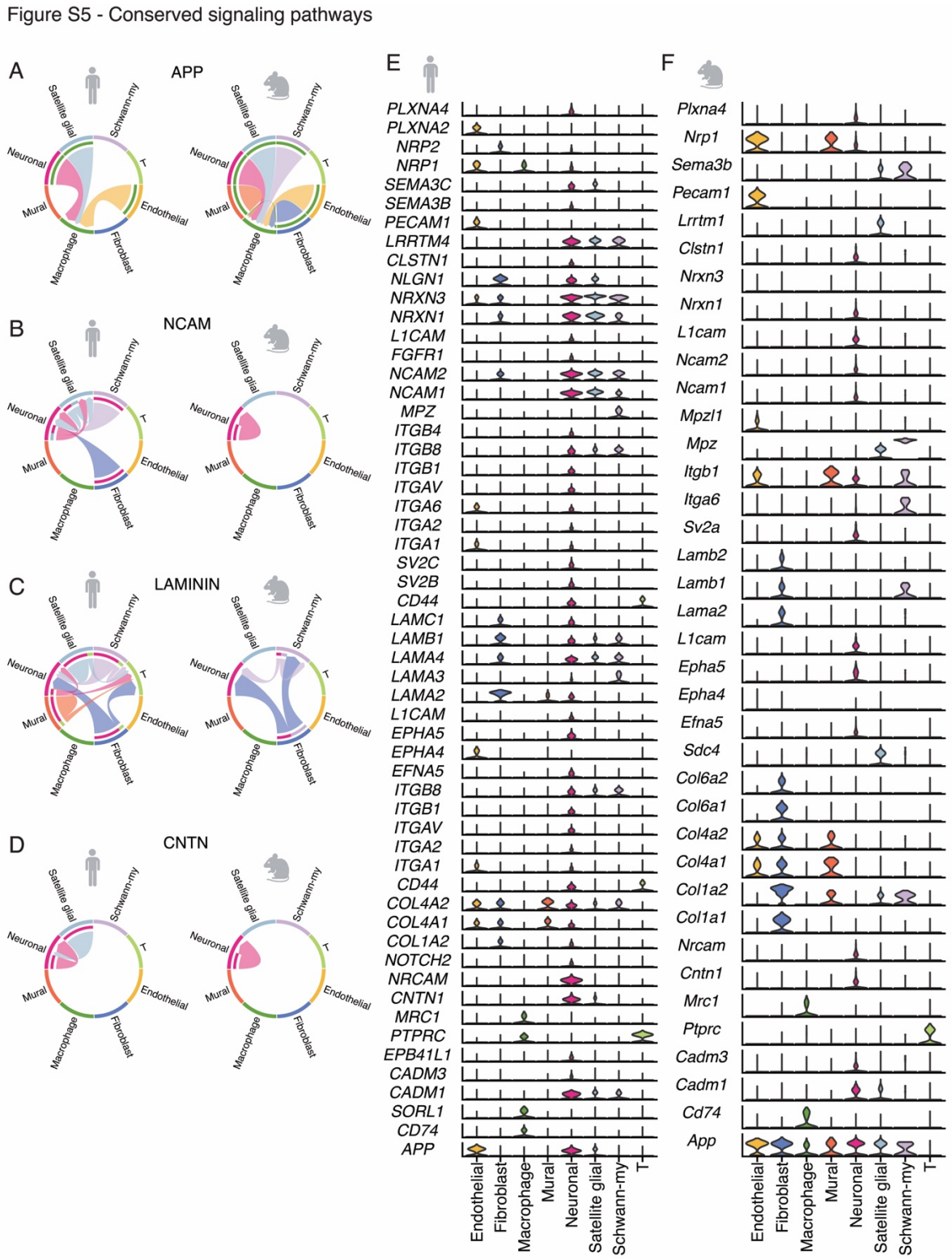

Figure S5.

A-D. Chord diagrams showing selected signaling pathways that are significantly enriched in both human (top) and mouse (bottom) snRNA-seq data. In the chord diagram, the inner thinner bar colors represent the targets that receive signals from the corresponding outer bar. The inner bar size is proportional to the signal strength received by the targets. **E** and **F**. Violin plots showing the expression level across cell types of genes associated with the conserved signaling pathways in human (B) and mouse (C). Violin plots are colored by cell types.

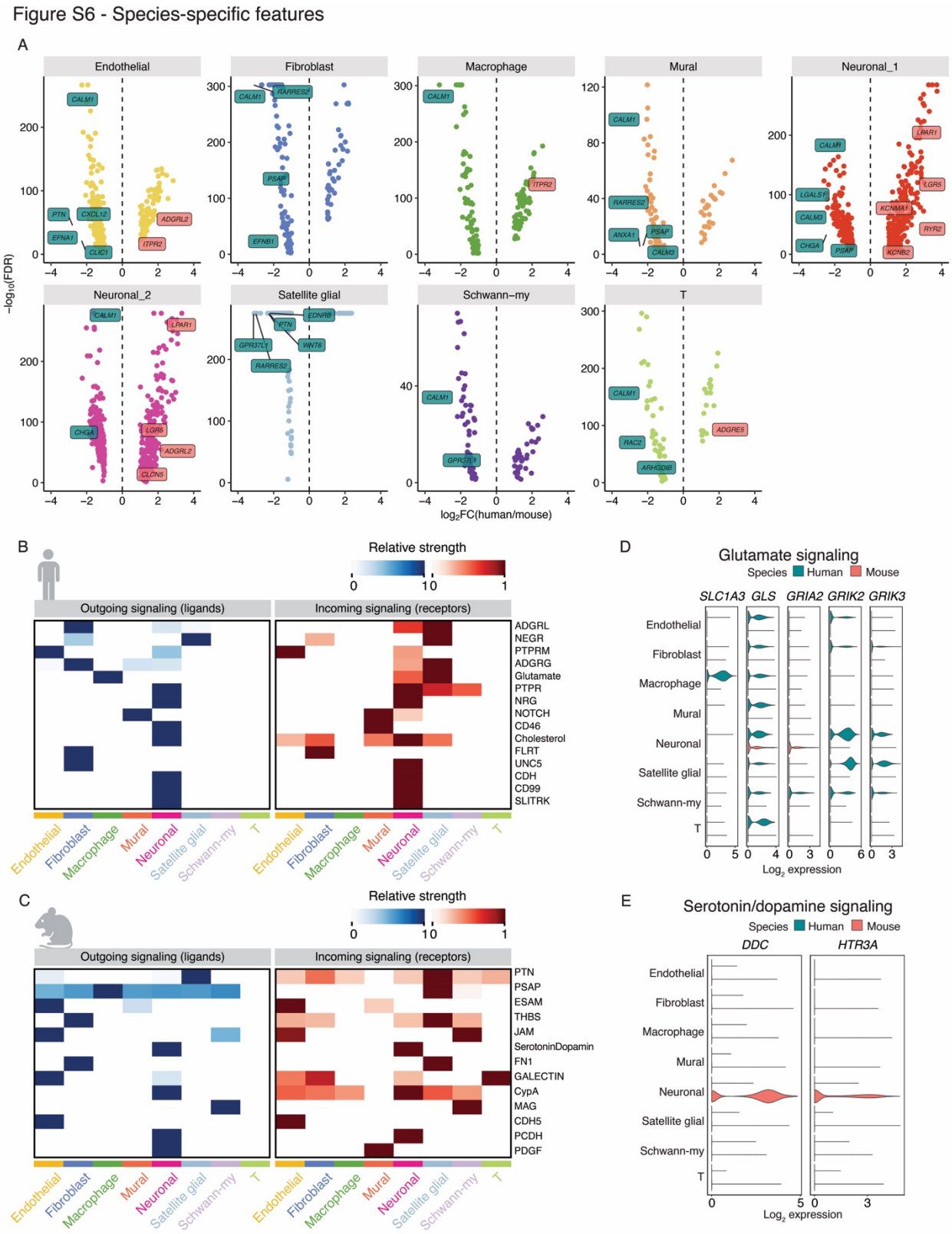

Figure S6.

A. Volcano plots showing the differentially expressed genes (Log2FC > 1 for mouse and Log2FC < (-1) for human, FDR < 0.05) in individual cell types between nuclei from mouse and human snRNA-seq data. Top 5 genes (sorted by Log2FC) of neuropeptides, neuropeptide receptors, GPCR, and ion channels are labeled. **B** and **C**. Heatmaps showing the relative strength of signaling pathways only enriched in human (B) or mouse (C) data. The strength of a signal pathway is normalized by the

maximal strength across all cell types in a given species. Outgoing signaling strength is calculated by aggregating the average expression of ligands associated with a given pathway in each cell type. Incoming signaling strength is calculated by aggregating the average expression of receptors associated with a given pathway in each cell type. **D** and **E**. Violin plots showing the expression level across all human and mouse cell types of genes associated with the glutamate signaling pathway (D) and serotonin/dopamine signaling pathway (E). Violin plots are colored by species.

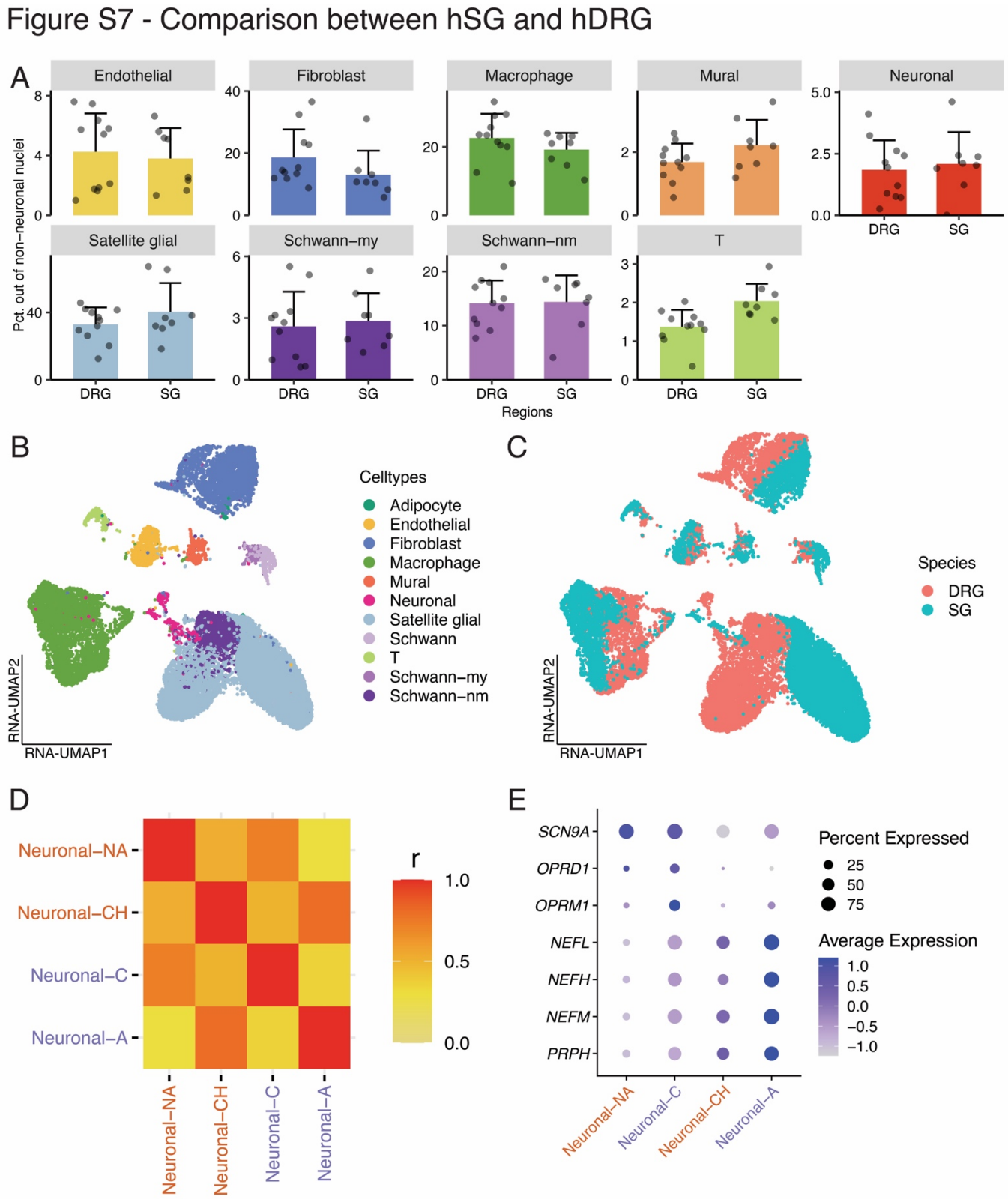

Figure S7.

A. Bar plot showing the cell type composition in human SG and DRG libraries. ($p = 0.91$ for endothelial cells, $p = 0.08$ for fibroblasts, $p = 0.24$ for macrophages, $p = 0.96$ for mural cells, $p = 0.28$ for neuronal (all neuronal clusters combined), $p = 0.93$ for satellite glial cells, $p = 0.97$ for schwann-my, $p = 0.3$ for schwann-nm, and $p = 1$ for T cells. Bonferroni-corrected student t-tests comparing percentages of a given cell type in human libraries to those in mouse libraries [*$p = 0.005$, **$p =$

0.0011, ***p = 0.00011]). **B and C.** Gene expression UMAP of human SG and DRG when clustering together without integration. 5,000 nuclei are randomly sampled per species. Nuclei are colored by transcriptional cell types (B) or ganglia (C). **D.** Heatmap showing the Pearson's correlation coefficient (r) by correlating the expression of cell-type-specific marker genes between human SG and DRG neuronal cell types. **E.** Dot plot showing the expression of selected genes shared between SG neuronal-NA and DRG neuronal-C, or SG neuronal-CH and DRG neuronal-A.

Figure S8 - glial cell quantification

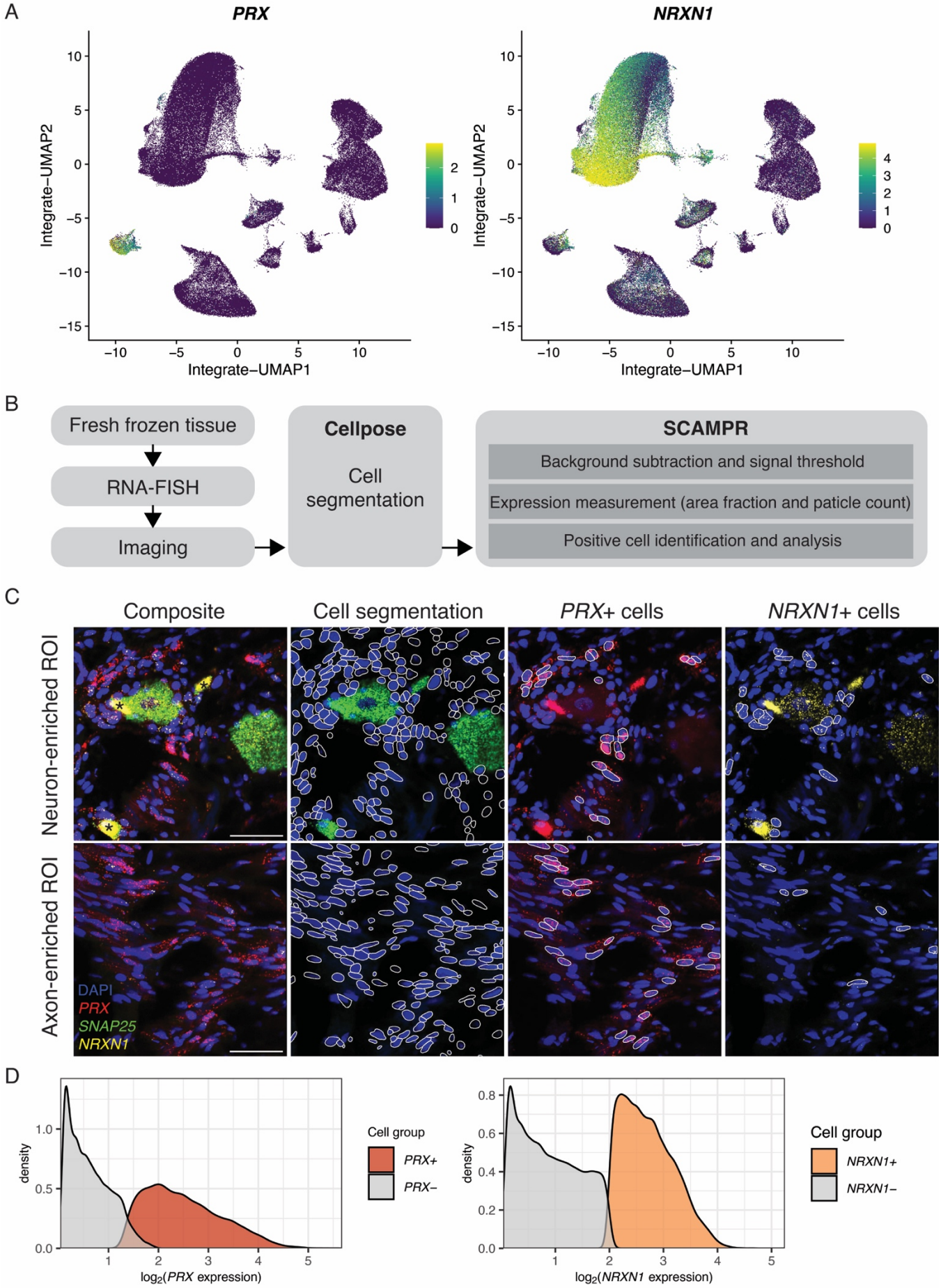

Figure S8.

A. Integrative gene expression UMAP of human SG and DRG showing the expression of myelinating schwann cell marker *PRX* (left) and satellite glial and non-myelinating schwann cell marker *NRXN1* (right). **B.** Workflow of RNA-FISH image analysis. **C.** Representative images demonstrating results of cell segmentation and calling of positive cells based on *PRX* and *NRXN1* expression. Scale bar = 50 um. **D.** Distribution of *PRX* and *NRXN1* expression in all expressing cells.

Figure S9 - Genomic regulatory networks

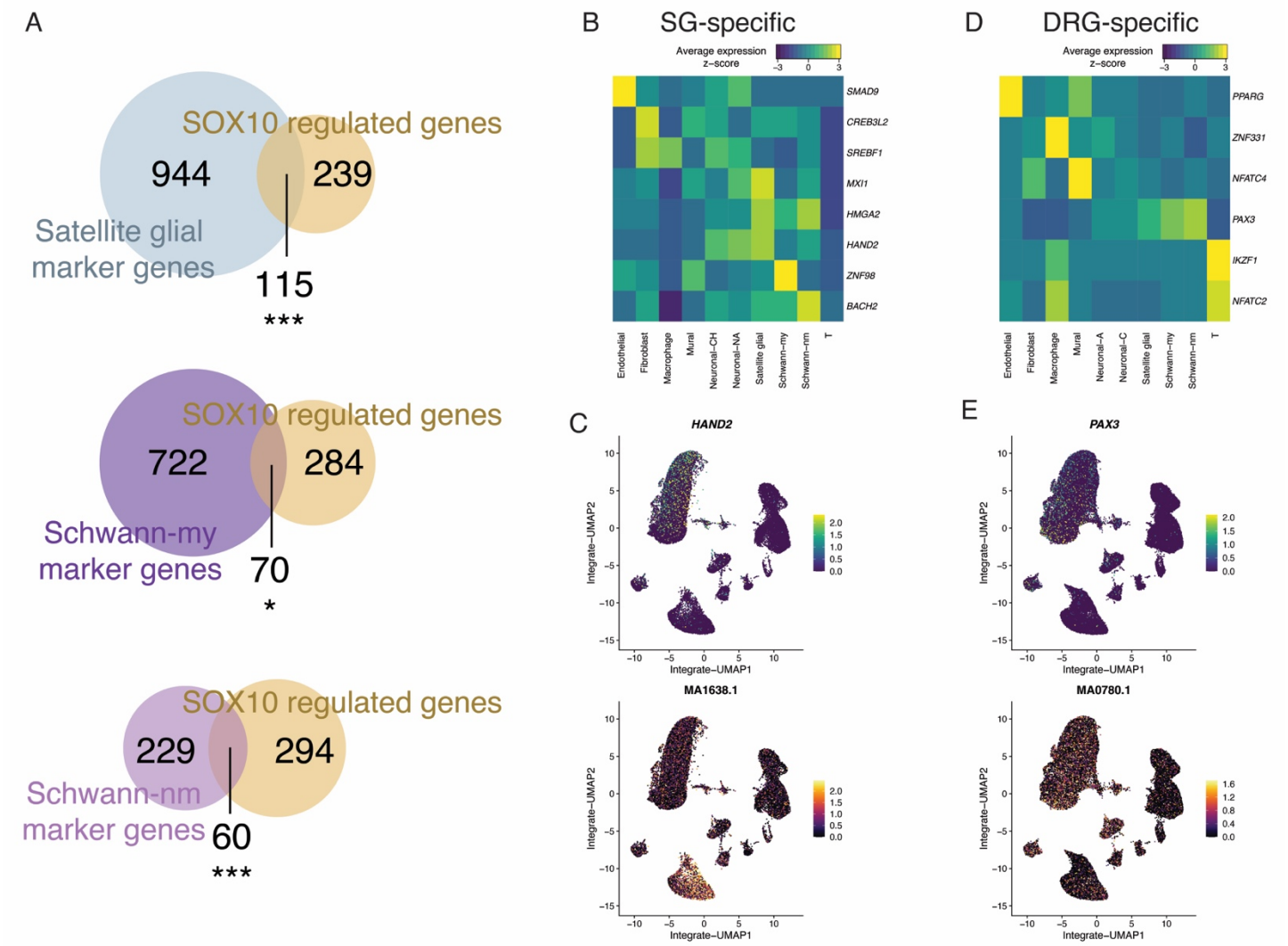

Figure S9

A. Overlap between SOX10-regulated genes with marker genes specific for satellite glial cells (top), myelinating schwann cells (mid), and non-myelinating schwann cells (bottom). Hypergeometric tests: p = 2.4E-8 [***] for satellite glial cells, p = 0.017 [*] for myelinating schwann cells, p = 1,2E-17 [***] for non-myelinating schwann cells. [*p = 0.05, ***p = 0.001] **B.** Heatmap showing the expression of SG-specific TFs in individual SG cell types. **C.** UMAPs showing *HAND2* gene expression (top) in snRNA-seq data and HAND2 motif enrichment (bottom) in snATAC-seq data from human SG. **D.** Heatmap showing the expression of DRG-specific TFs in individual DRG cell types. **E.** UMAPs showing *PAX3* gene expression (top) in snRNA-seq data and PAX3 motif enrichment (bottom) in snATAC-seq data from human DRG.

Figure S10 - Subtype annotation of macrophage subtypes

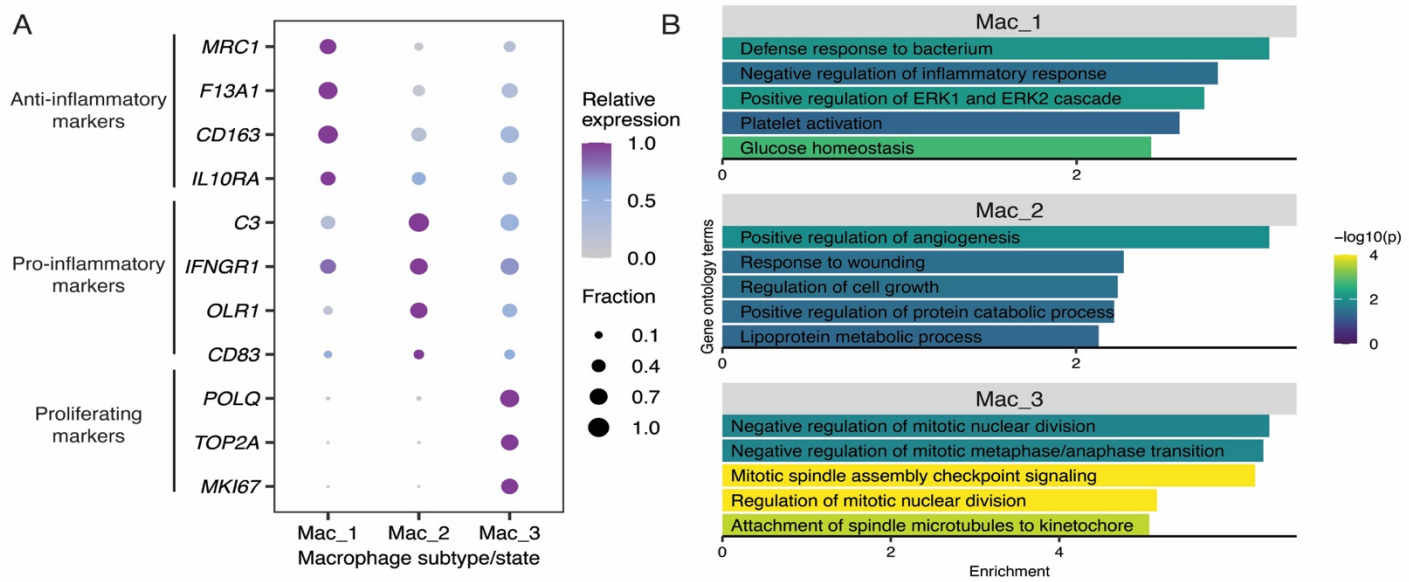

Figure S10

A. Dot plot displaying the expression of marker genes in individual macrophage subtypes. Dot size denotes the fraction of nuclei expressing a marker gene (>0 counts), and color denotes relative expression of a gene in each macrophage subtype (calculated as the mean expression of a gene relative to the highest mean expression of that gene across all cell types). **B.** Top gene ontology terms enriched in each macrophage subtype.

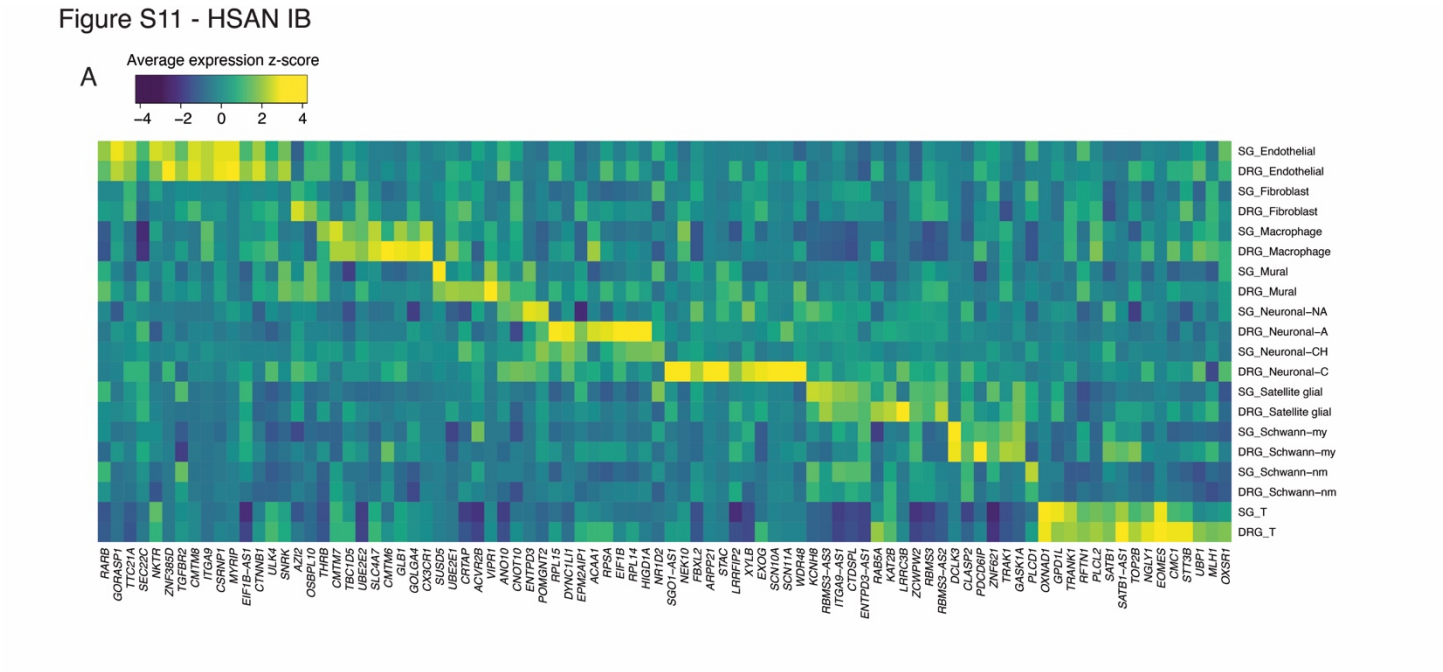

Figure S11

A. Heatmap showing the expression pattern of genes in 3p24-22 that are also expressed in any cell types in human SG and DRG snRNA-seq data.